UNIVERSIDADE FEDERAL DO RIO GRANDE DO SUL
PROGRAMA DE PÓS-GRADUAÇÃO EM FÍSICA
Tese de Doutorado

Gus Ourique

Numerical Simulation of Cell Aspiration by Micropipette (Simulação Numérica de Aspiração de Células por Micropipeta)

Porto Alegre, Brasil
29 de abril de 2024

Gus Ourique

Numerical Simulation of Cell Aspiration by Micropipette
(Simulação Numérica de Aspiração de Células por Micropipeta)

Tese submetida ao Programa de Pós-Graduação em Física do instituto de Física da UFRGS, como quesito parcial para obtenção do título de Doutor em Física.

Supervisor: Leonardo Gregory Brunnet

Porto Alegre, Brasil

29 de abril de 2024

Gus Ourique

Numerical Simulation of Cell Aspiration by Micropipette (Simulação Numérica de Aspiração de Células por Micropipeta)

Tese submetida ao Programa de Pós-Graduação em Física do instituto de Física da UFRGS, como quesito parcial para obtenção do título de Doutor em Física.

Leonardo Gregory Brunnet
Orientador

C1
Convidado 1

C2
Convidado 2

C3
Convidado 3

C4
Convidado 4

Porto Alegre, Brasil
29 de abril de 2024

Abstract

Cells form the fundamental building blocks of living organisms, and understanding the mechanical properties of the tissues they form has significant implications in cancer progression, wound healing and embryology. In this study, we present a two-dimensional model where each cell consists of particles connected by springs, working as perimeter forces, and a second term playing a role of area conservation. The purpose of our research is to investigate the mechanical parameters compatible with the micropipette aspiration of a group formed with these cells, and relate them with the macroscopic behavior of a tissue. To validate the accuracy of our cellular model, we conducted micropipette aspiration simulations on single cells. Our results demonstrate that a one-dimensional mechanical model can effectively describe the behavior of single cells. This finding suggests that macroscopic measures, such as cell stretch, can be used to extract microscopic cell parameters. Interestingly, we also observed that cellular activity does not significantly influence the mechanical properties of cells in this particular scenario. Moving beyond single cells, we extended our simulations to cell aggregates to explore their internal parameters. By subjecting cell aggregates to micropipette aspiration, we were able to map internal parameters that could potentially be applied to real cells. We found that, in our model, cellular adhesion does not impact the speed of viscous flow unless it is strong enough to completely obstruct the flow. Furthermore, we discovered a linear correlation between the minimum aspiration pressure required for cell aggregates to be aspirated in a continuous viscous-plastic flow and the strength of cell membrane adhesion. This finding highlights the potential importance of considering adhesive properties when studying cell aggregates and their behavior under force. In conclusion, our research contributes novel insights into the mechanical parameters of tissues, enhancing our understanding of cell tissue dynamics.

Keywords: cell movement; micropipette; cell simulation.

Resumo

As células formam os blocos de construção fundamentais dos organismos vivos e entender as propriedades mecânicas dos tecidos que elas formam tem implicações significativas na progressão do câncer, na cicatrização de feridas e na embriologia. Neste estudo, apresentamos um modelo bidimensional onde cada célula consiste em partículas conectadas por molas, funcionando como forças de perímetro, e um segundo termo desempenhando o papel de conservação de área. O objetivo deste trabalho é investigar os parâmetros mecânicos compatíveis com a aspiração por micropipeta de um grupo formado por essas células e relacioná-los com o comportamento macroscópico de um tecido. Para validar a precisão de nosso modelo celular, realizamos simulações de aspiração por micropipeta em células individuais. Nossos resultados demonstram que um modelo mecânico unidimensional pode descrever efetivamente o comportamento de células individuais. Esse achado sugere que medidas macroscópicas, como estiramento celular, podem ser usadas para extrair parâmetros celulares microscópicos. Também observamos que a atividade celular não influencia significativamente as propriedades mecânicas das células neste cenário específico. Indo além das células individuais, estendemos nossas simulações para agregados celulares para explorar seus parâmetros internos. Ao submeter agregados celulares à aspiração por micropipeta, pudemos mapear parâmetros internos que poderiam ser potencialmente aplicados a células reais. Descobrimos que em nosso modelo a adesão celular não impacta a velocidade do fluxo viscoso a menos que seja forte o suficiente para obstruí-lo completamente. Além disso, descobrimos uma correlação linear entre a pressão mínima de aspiração necessária para que os agregados celulares sejam aspirados em um fluxo viscoplástico contínuo e a força de adesão da membrana celular. Esse resultado destaca a importância de considerar as propriedades adesivas ao estudar agregados celulares e seu comportamento sob força. Em conclusão, nosso estudo contribui com novos insights sobre os parâmetros mecânicos de tecidos, aprimorando a compreensão da dinâmica de tecidos celulares.

Press Release

Exploring Mechanical Properties of Cell Tissues: Insights from Simulation Studies

Cells constitute the fundamental units of living organisms, and deciphering the mechanical properties of the tissues they form is primordial for understanding various biological processes such as cancer progression, wound healing, and embryology. In this study, we introduce a two-dimensional model representing cells as particles interconnected by springs, with perimeter forces and area conservation terms. Our investigation aims to elucidate the mechanical parameters relevant to micropipette aspiration and their implications for tissue behavior.

Through simulations, we demonstrate the efficacy of a simplified one-dimensional mechanical model in describing the behavior of single cells. Remarkably, we observe minimal influence of cellular activity on the mechanical properties in this specific context. Expanding our analysis to cell aggregates, we uncover a significant relationship between the minimum aspiration pressure required for cell aggregates to undergo continuous viscous-plastic flow and the strength of cell membrane adhesion. This highlights the critical role of adhesive properties in determining the behavior of cell aggregates under external forces.

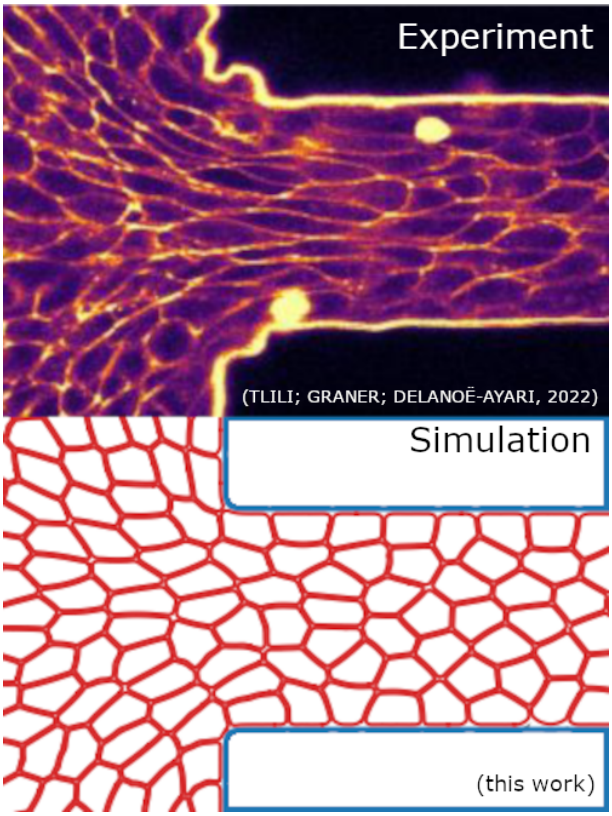

Comparison of the experiment (TLILI; GRANER; DELANOE-AYARI, 2022) (top) and simulations conducted in this study (bottom).

Our findings not only provide valuable insights into the mechanical characteristics of tissues but also offer a framework for understanding the interplay between cellular mechanics and tissue dynamics. By bridging the gap between microscopic cellular parameters and macroscopic tissue behavior, our research contributes to advancing our understanding of fundamental biological processes and lays the groundwork for future studies in tissue biomechanics and related fields.

Keywords: tissue mechanics; micropipette absorption; extended cell model simulation.

List of Figures

Contents

1 Introduction

Throughout the centuries, biological science has progressively advanced in the examination of living organisms and their attributes, whether they be microscopic, such as cellular behavior, or macroscopic, encompassing the arrangement of animals and organisms. In recent times, additional scientific disciplines have begun focusing in the exploration and delineation of biological properties from alternative perspectives, creating domains such as biological physics.

Biological physics finds its origins in the adaptation of physical principles to explain phenomena such as the collective motion of birds and fishes (REYNOLDS, 1987; COUZIN et al., 2005; SUMPTER et al., 2008; GUTTAL; COUZIN, 2010), as well as human pedestrians (HELBING; MOLNÁR, 1995; OBATA et al., 2000). Furthermore, mechanical attributes inherent in living entities, exemplified by bacteria (BERG; TURNER, 1979), individual cells (HOCHMUTH, 1993), and cellular aggregates (GUEVORKIAN et al., 2010; GUEVORKIAN et al., 2011; GUEVORKIAN; MAÎTRE, 2017), stand as subjects of inquiry within this facet of physics. Specifically, the exploration of dynamic and mechanical characteristics pertaining to cells has engendered substantial enthusiasm among biological physics physicists, as these traits generate insights into wound healing, inflammatory responses, and even tumor metastasis (HAGA et al., 2005).

Although the targets within the domain of biological physics exhibit discernible disparities, they collectively share a fundamental attribute: that of self-propulsion. Diverging from entities delineated by classical physics, self-propelled entities possess the capability to engender motion through the utilization of intrinsic energy, whether it is stored internally or acquired from the immediate surroundings. Adopting a particle-based perspective upon these entities, it is plausible to assert that this internal energy modifies the particle dynamics, thereby creating a state of persistent non-equilibrium systems, a state which diverges from the equilibrium frameworks described by classical physics (RAMASWAMY, 2010).

Owing to this intrinsic energy facilitating motion, we commonly denominate such entities as “active particles”. Illustrative instances of active particles encompass boids and active Brownian particles.

Boids represent a category of particles originally conceived to replicate the collective motion exhibited by biological entities such as birds, herds, or fish (REYNOLDS, 1987). The term “boid” derives from the English word “bird-oid”, a contraction of "bird-like," signifying resemblance to avian locomotion. The dynamics governing boid behavior are simple and can be described by three primary constituents: spacing, alignment, and

cohesion. In essence, the movement orientation of an individual boid within a system of multiple boids tends to synchronize with the orientations of its neighbors. Furthermore, the boid endeavors to maintain proximity to its neighbors while avoiding direct contact.

The concept underlying active Brownian particles, in contrast, deviates somewhat from the aforementioned. Classical Brownian particles exhibit an inherent degree of internal randomness, often stemming from collisions with smaller particles present within the environment, thereby predominantly engendering diffusive motion (EINSTEIN, 1905). Nonetheless, active Brownian particles, in addition to their innate diffusion, feature an orientation parameter that evolves stochastically. This orientation influences the particle's movement, giving rise to a preferred trajectory in tandem with natural diffusion (ROMANCZUK et al., 2012)

The employment of active Brownian particles in biological physics is commonly intertwined with the characterization of the particles' orientation parameter. In elucidating the collective movement of cells, Szabó et al. (2006) engineered the orientation angle of their active Brownian particles to align with the resultant force acting upon each particle. Moreover, they incorporated a force acting at short distances to attract particles and, at even closer distances, to repel them. The outcome of this amalgamation of alignment and adhesion mechanisms is the induction of concerted motion among multiple particles following contact, leading to coordinated movement in a shared direction. This approach effectively emulates experiments conducted with actual cells (SZABÓ et al., 2006).

A constraint inherent in models portraying cells as individual particles lies in the notion of shape. Actual cells typically exhibit behavior akin to viscoelastic solids (JONES et al., 1999), enabling deformations in their morphology. In light of this, it is anticipated that the individual particle model would fall short in faithfully replicating the elastic attributes intrinsic to cellular entities.

To circumvent this constraint, more intricate models accounting for additional elements have been developed over the years, such as the Voronoi model, vertex model, Potts model, and multiparticle model. The Voronoi model (SULSKY; CHILDRESS; PERCUS, 1984), while still encompassing the notion of individual particles, incorporates supplementary forces based on the Voronoi cells generated by particle tessellation. This approach introduces forces linked to cell volume and perimeter. Similarly, the vertex model (WELIKY; OSTER, 1990) also employs Voronoi tessellation to integrate extra forces; however, in this case, these forces act directly upon the vertices of the Voronoi tessellation rather than on the central particle. Both the Voronoi and vertex models share a limitation in terms of accurately depicting irregular cell shapes. Since Voronoi tessellation inherently produces lattice-like cells, elongated or curvilinear cellular forms cannot be faithfully reproduced by this method, thereby restricting the portrayal of experiments involving substantial cell distortions. In contrast, the Potts model employs a discretization of space

into boxes (typically pixels in 2D (GLAZIER; GRANER, 1993) or voxels in 3D (SWAT et al., 2012)), endowing each box with a comprehensive description of its physical properties. Temporal evolution is achieved using Monte Carlo steps, determining the state that minimizes the system's energy. In the context of the cellular Potts model (GRANER; GLAZIER, 1992), each box bears information about its cell affiliation. Constraints are directly imposed within the system's Hamiltonian, ensuring specific properties, such as the absence of disassociated boxes from the cell body, preservation of approximate cell volume and perimeter constancy, among others. This model adeptly characterizes cellular movement (FORTUNA, 2020) and avoids the shape limitation encountered in the Voronoi and vertex models. However, due to the Monte Carlo temporal advancement, temporal information is not fully resolved, necessitating recovery via estimations and relationships between temporal dynamics and Monte Carlo dynamics (BILLONI; STARIOLO, 2007).

The multiparticle model involves the construction of a composite body by interlinking multiple individual particles. An illustrative instance of this modeling approach was demonstrated by J. Newman (2005), where artificial cells were fabricated by assembling numerous randomly positioned and interconnected particles. This methodology resulted in the creation of artificial cells characterized by a simplified internal structure.

In order to describe objects possessing elasticity using multiparticle models, a strategy involves the creation of multiple particles arranged in a periodic manner and interconnected by springs (ÅSTRÖM; LATVA-KOKKO; TIMONEN, 2003). This approach, initially introduced as a framework capable of characterizing cellular membranes (ÅSTRÖM; KARTTUNEN, 2006), owing to its simplicity, accommodates the inclusion of supplementary features in these models, such as cell division (MKRTCHYAN; ÅSTRÖM; KARTTUNEN, 2014) or activity (TEIXEIRA; FERNANDES; BRUNNET, 2021). To extract mechanical parameters of cells, it is imperative to subject the cells to a force and observe their response (HOCHMUTH, 2000).

An interesting experiment for determining the elastic properties of cells is the micropipette aspiration experiment. This experimental procedure involves bringing a micropipette into proximity with a cellular body, whether it be a single cell or a cell aggregate, and applying pressure to induce aspiration. The aspirated cellular body deforms, facilitating subsequent measurements. The micropipette aspiration experiment has been utilized since 1970 (GONZÁLEZ-BERMÚDEZ; GUINEA; PLAZA, 2019) to measure physical properties of cells. It has been employed for quantifying the elastic properties of red blood cells (EVANS, 1973), the viscous properties of adhesive cells (SATO et al., 1990), and the elastic properties of the cell nucleus (GUILAK; TEDROW; BURGKART, 2000). More recently, this technique has also been applied to assess the elastic, viscous, and rheological properties of tissues (GUEVORKIAN et al., 2011), and it can even be used for *in vivo* measurements (NAVA et al., 2008; MAJKUT et al., 2013; PORAZINSKI

et al., 2015; GUEVORKIAN; MAÎTRE, 2017). Due to its ability to induce continuous deformation in cells or tissues (GUEVORKIAN et al., 2010) and its compatibility with *in vivo* systems, this approach has gained prominence over classical techniques like parallel plate compression, where cells merely relax towards equilibrium.

In conjunction with micropipette aspiration experiments, analytical models have been devised to establish correlations between the measurable outcomes of the experiments and the physical properties of the investigated cellular entity. Initially, Theret et al. (1988) proposed a half-space model to delineate the elastic properties of the entity in relation to its deformation length, i.e., the extent of the cell membrane encompassed within the micropipette. More intricate models have been developed to provide a slightly more detailed description of the micropipette aspiration experiment (WU; HERZOG; EPSTEIN, 1999; HOCHMUTH, 2000; PLAZA et al., 2015). Nevertheless, these analytical models are constrained to equilibrium solutions of symmetric membranes and are incapable of capturing phenomena such as deformations or changes in neighboring configurations (OURIQUE; TEIXEIRA; BRUNNET, 2022).

In order to surmount the limitations inherent in analytical models, numerical models designed to describe cells and tissues have been adapted to encompass the micropipette aspiration experiment. Boey, Boal e Discher (1998) introduced a numerical model depicting cells as interconnected points within a three-dimensional space, which was subsequently employed to simulate the micropipette aspiration experiment (DISCHER; BOAL; BOEY, 1998). This model demonstrated consistency in replicating cell elastic properties; however, its evolution was facilitated through Monte Carlo steps, restricting its applicability to stationary scenarios. More sophisticated models of the micropipette aspiration experiment have been developed (ZHOU; LIM; QUEK, 2005; ESTEBAN-MANZANARES et al., 2017), including considerations for the cytoskeleton (LYKOV et al., 2017).

In this study, our aim is to devise a numerical model for simulating the micropipette aspiration experiment on cells. Our approach diverges from the precedents set by previous models (DISCHER; BOAL; BOEY, 1998; ZHOU; LIM; QUEK, 2005; ESTEBAN-MANZANARES et al., 2017; LYKOV et al., 2017). We have formulated a minimalist model that not only emulates the mechanical properties of cells but also takes advantage of active particle dynamics. In our model, we extend its application to multiple cell systems, employing non-active particles in this scenario.

The employed model constitutes an expansion of the framework introduced by Teixeira, Fernandes e Brunnet (2021), enhanced by the incorporation of supplementary features including volume conservation, wall interactions, and interplay among distinct membranes. Due to its minimalist nature, this model facilitates simulations involving multiple interacting membranes, akin to experiments involving the aspiration of cell aggregates (GUEVORKIAN et al., 2010; GUEVORKIAN et al., 2011).

With the outlined model, we conducted simulations of both individual cell aspiration and cell aggregate aspiration. The ensuing outcomes will be elucidated in the subsequent sections.

In Section 2, we provide a literature review on cell modeling and aspiration. In Section 3, we describe our numerical model. Section 4 details our simulations. Section 5 presents the results obtained from our simulations. Finally, in Section 6, we draw conclusions from this work.

2 Review

In this chapter, we will present the most common theoretical description for the single-cell aspiration experiment, along with one of the possible descriptions used to characterize aggregates.

2.1 Single Cell

The cell aspiration experiments using micropipette, initially conducted on individual cells, typically rely on the theoretical framework proposed by Theret et al. (1988). They adopted a half-space model to depict a cell and brought it into proximity with a cylindrical micropipette. This can be understood as an infinitely large cell occupying half of the entire physical space, with the unoccupied region hosting a micropipette in contact with the cell.

Figure 1 depicts a schematic of this model, in this case featuring a micropipette with inner radius a, outer radius b, and aspiration pressure ΔP. In order to organize future

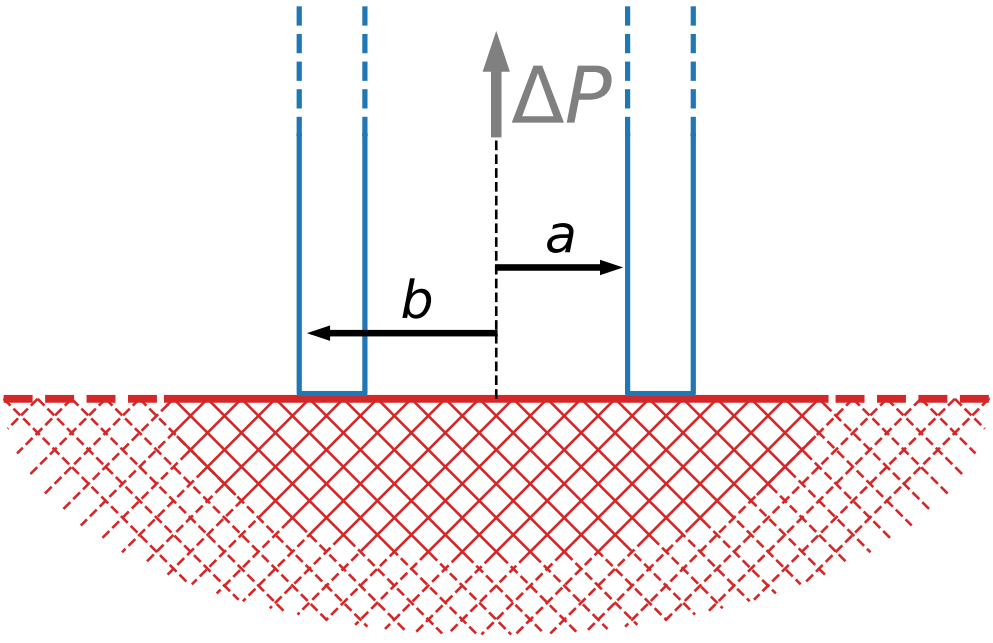

Figure 1 – Schematic of the half-space model employed to describe the micropipette aspiration experiment. The micropipette walls are depicted in blue, the cell body in red, and the vector associated with the pressure-induced force in gray. Dashed lines indicate infinite extensions of the system, illustrating that, in this model, the cell body occupies half of the entire space. Parameter a represents the inner radius of the micropipette cylinder, while b represents the outer radius.

explanations, we define the z-axis as the axis coinciding with the center of symmetry of the micropipette. Consequently, the r-axis is perpendicular to the z-axis and is aligned with the entrance of the micropipette.

To address the present problem, Theret et al. (1988) considered two distinct and independent boundary conditions:

1) The first assumption establishes that the membrane pressure on the edge of the pipette (the ring with area $\pi(b^2 - a^2)$) remains constant. In other words, it assumes that the component s_{zz} of the stress tensor remains constant over this ring. For equilibrium to hold, the force component generated by s_{zz} on the pipette edge and the force produced by the pressure ΔP on the circular area with radius a inside the pipette must be equal, that is,

$$s_{zz} = -\frac{a^2}{b^2 - a^2}\Delta P \ . \tag{2.1}$$

2) The second boundary condition asserts that the deformation of the membrane in the z-direction, $u_z(r, 0)$, is zero over the surrounding ring.

$$u_z(r, 0) = 0 \ , \quad a < r < b \ . \tag{2.2}$$

Now, with the boundary conditions established, and assuming that the body being modeled is composed of a completely elastic and incompressible medium, we have four expressions that rules deformation, namely:

$$\begin{aligned} \nabla \cdot \mathbf{s} &= 0 && (2.3)\\ \frac{1}{2}[\nabla\vec{u} + (\nabla\vec{u})^T] &= \mathbf{e} && (2.4)\\ \nabla\vec{u} &= 0 && (2.5)\\ -p\mathbf{I} + 2\mu\mathbf{e} &= \mathbf{s} \ , && (2.6) \end{aligned}$$

where $\mathbf{s}$ is the stress tensor, $\vec{u}$ is the displacement vector, $\mathbf{e}$ is the infinitesimal strain tensor, p is the mean stress, $\mathbf{I}$ is the identity tensor, and μ is associated with the elastic modulus E, with $\mu = E/3$. Equation 2.3 is the stress equilibrium condition for a deformed body (LANDAU; LIFCHTZ, 1967), and Equation 2.4 relates the infinitesimal strain tensor to the displacement gradient. On the other hand, Equation 2.5 is connected to material incompressibility, and Equation 2.6 provides the stress-strain relationship for an incompressible material.

Theret et al. (1988) solved the system of equations for both boundary conditions and obtained as a solution,

$$L_p = \frac{3a\Delta P}{2\pi E}\Phi \ , \tag{2.7}$$

where L_p is the total membrane length inside the pipette along its axis, Φ is a dimensionless number that depends on the geometry of the micropipette walls (parameters a and b in Figure 1) and the type of boundary condition. In their work, Theret et al. (1988) chose to use a value of Φ close to 2.1, as it was a consistent value for both boundary conditions.

2.2 Cell Aggregate

For cellular aggregates, we have a comprehensive description proposed by Tlili et al. (2015), where the system is described by combining intra-cellular viscoelasticity with inter-cellular plasticity, as illustrated in Figure 2.

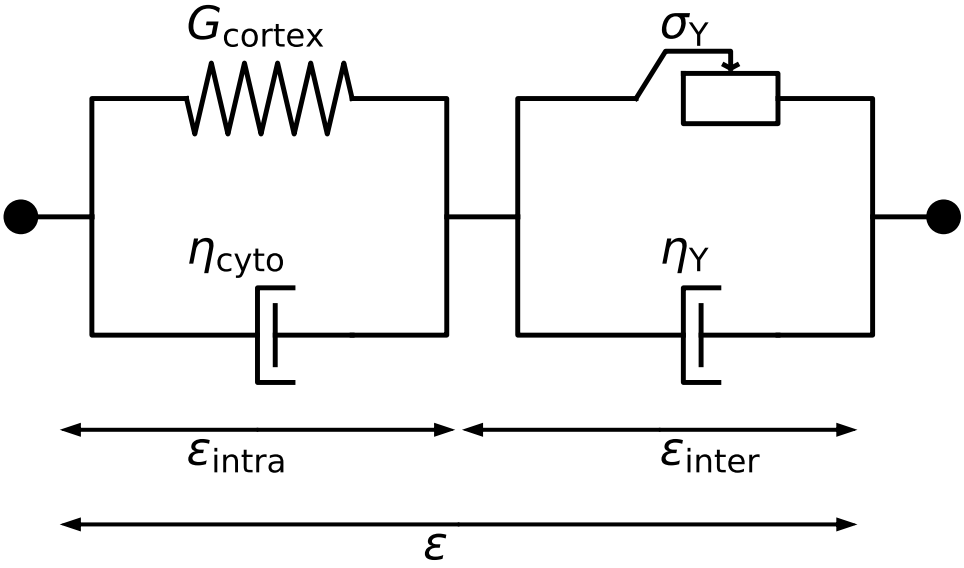

Figure 2 – Proposed cellular aggregate rheological model. This model consists in an intra-cellular rheology model combined with an inter-cellular rheological one.

In this Figure, the left side illustrates the Kelvin-Voigt element, which characterizes the cellular components within the aggregate. Here, G_{cortex} signifies the effective shear elastic modulus of the cell, and η_{cyto} denotes the viscosity of the cytoplasm. On the right side, we present the rheological component of the cell aggregate, wherein σ_Y represents the yield stress of the aggregates, microscopically associated to cell rearrangement, while η_Y is the viscosity.

This model exhibits interesting properties, such as an intrinsic resistance to deformation, causing the aggregate to only start flowing after reaching a certain minimum pressure. We describe the model in a one-dimensional framework for deformations using the dissipation function formalism (TLILI et al., 2015),

$$\mathcal{E}(\varepsilon, \varepsilon_{\text{intra}}) = \frac{1}{2} G_{\text{cortex}} \varepsilon_{\text{intra}}^2 \tag{2.8}$$

$$\mathcal{D}(\varepsilon, \varepsilon_{\text{intra}}) = \frac{1}{2} \eta_{\text{cyto}} \dot{\varepsilon}_{\text{intra}}^2 + \frac{1}{2} \eta_{\text{Y}} \left(\dot{\varepsilon} - \dot{\varepsilon}_{\text{intra}}\right)^2 + \sigma_{\text{Y}} \left|\dot{\varepsilon} - \dot{\varepsilon}_{\text{intra}}\right| \tag{2.9}$$

where $\mathcal{E}$ describes the system's elastic energy, and $\mathcal{D}$ represents the dissipation.

Following the dissipation function formalism, we obtain the stress, σ:

$$\sigma = \frac{\partial \mathcal{D}}{\partial \dot{\varepsilon}} + \frac{\partial \mathcal{E}}{\partial \varepsilon} \tag{2.10}$$

When applied to equations 2.8 and 2.9, we obtain,

$$\sigma = \eta_{\text{Y}} \left(\dot{\varepsilon} - \dot{\varepsilon}_{\text{intra}}\right) + \sigma_{\text{Y}} \frac{\dot{\varepsilon} - \dot{\varepsilon}_{\text{intra}}}{\left|\dot{\varepsilon} - \dot{\varepsilon}_{\text{intra}}\right|} \tag{2.11}$$

$$0 = G_{\text{cortex}} \varepsilon_{\text{intra}} + \eta_{\text{cyto}} \dot{\varepsilon}_{\text{intra}} - \eta_{\text{Y}} \left(\dot{\varepsilon} - \dot{\varepsilon}_{\text{intra}}\right) - \sigma_{\text{Y}} \frac{\dot{\varepsilon} - \dot{\varepsilon}_{\text{intra}}}{\left|\dot{\varepsilon} - \dot{\varepsilon}_{\text{intra}}\right|} \tag{2.12}$$

Note that $\left(\dot{\varepsilon} - \dot{\varepsilon}_{\text{intra}}\right) = \dot{\varepsilon}_{\text{inter}} = 0$ when $\sigma < \sigma_{\text{Y}}$, dividing the system into two distinct regimes. In this case, the system is simply described by the following expression:

$$\eta_{\text{cyto}} \dot{\varepsilon}_{\text{intra}} + G_{\text{cortex}} \varepsilon_{\text{intra}} - \sigma = 0 \tag{2.13}$$

Which can be solved as a function of time, yielding:

$$\varepsilon_{\text{intra}} = \frac{\sigma}{G_{\text{cortex}}} \left(1 - e^{-\frac{t}{\tau_c}}\right) \tag{2.14}$$

where $\tau_c = \eta_{\text{cyto}} / G_{\text{cortex}}$. This expression indicates that, under these conditions, the system behaves purely elastically, deforming up to a limit defined by the elasticity of the aggregate. Note that in this particular case, the total aggregate displacement is equal to the internal cell displacement, i. e., $\varepsilon_{\text{intra}} = \varepsilon$

For the case where $\sigma > \sigma_{\text{Y}}$, the applied stress is sufficient to break the bonds between the cells, allowing flow into the pipette. To solve this case, we initially isolate the displacement variation in Equation 2.11

$$\eta_{\text{Y}} \left(\dot{\varepsilon} - \dot{\varepsilon}_{\text{intra}}\right) = \sigma - \sigma_{\text{Y}} \tag{2.15}$$

$$\dot{\varepsilon} = \frac{\sigma - \sigma_{\text{Y}}}{\eta_{\text{Y}}} + \dot{\varepsilon}_{\text{intra}} \tag{2.16}$$

and integrate with respect to time, resulting in:

$$\varepsilon = \frac{\sigma - \sigma_{\text{Y}}}{\eta_{\text{Y}}} t + \varepsilon_{\text{intra}} \,. \tag{2.17}$$

Finally, we substitute the solution obtained in Equation 2.14 into Equation 2.17, resulting in the solution:

$$\varepsilon = \frac{\sigma - \sigma_{\mathrm{Y}}}{\eta_{\mathrm{Y}}} t + \frac{\sigma}{G_{\mathrm{cortex}}} \left(1 - e^{-\frac{t}{\tau_c}}\right) \ . \tag{2.18}$$

The solution in Equation 2.18 is interesting as it highlights both the elastic and visco-plastic regimes, where the system flows while undergoing deformations.

3 Numerical Model

The numerical description model adopted in this work is an extension of the model presented by Teixeira, Fernandes e Brunnet (2021). It represents the cell membrane as a collection of active particles connected to form an extended body. Our extension includes volume conservation elements, modifies the contact interaction, and incorporates an adhesion and contact force for interaction between distinct membranes.

In the following sections, we will discuss in detail the equations describing the single-cell model (Section 3.1), the cell aggregate model (Section 3.2), the interaction with walls (Section 3.3), and the employed dynamics (Section 3.4).

3.1 Single Cell

The model incorporates four interactions to describe an individual cell: binding interaction, bending interaction, contact interaction, and area conservation.

3.1.1 Binding Interaction

Similar to the model presented by Teixeira, Fernandes e Brunnet (2021), the binding interaction is achieved through springs connecting the particles composing the membrane. The potential associated with this interaction, denoted as U_s, is given by:

$$U_s = \frac{k_s}{2} \sum_{i=1}^{N} (|\vec{d}_{i,i+1}| - d_0)^2 \tag{3.1}$$

where k_s is the spring stiffness, N is the number of particles in the membrane, $d_{i,j}$ is the distance between particle with index i and particle with index j of the membrane, and d_0 is the equilibrium distance of the spring. Note that, since we are in a periodic boundary situation, the particle with index N will interact with the particle with index 1.

In Figure 3, we have a sketch of an extended body composed of 50 particles connected by springs, representing a membrane. On the right side of the figure, there is an enlarged region of the membrane, highlighting the connecting springs, their equilibrium length, and stiffness. For convenience, we define,

$$d_0 = \frac{2\pi r_0}{N} \, . \tag{3.2}$$

This definition ensures that if the system is in a circular shape and in equilibrium, the cell's radius will be equal to r_0.

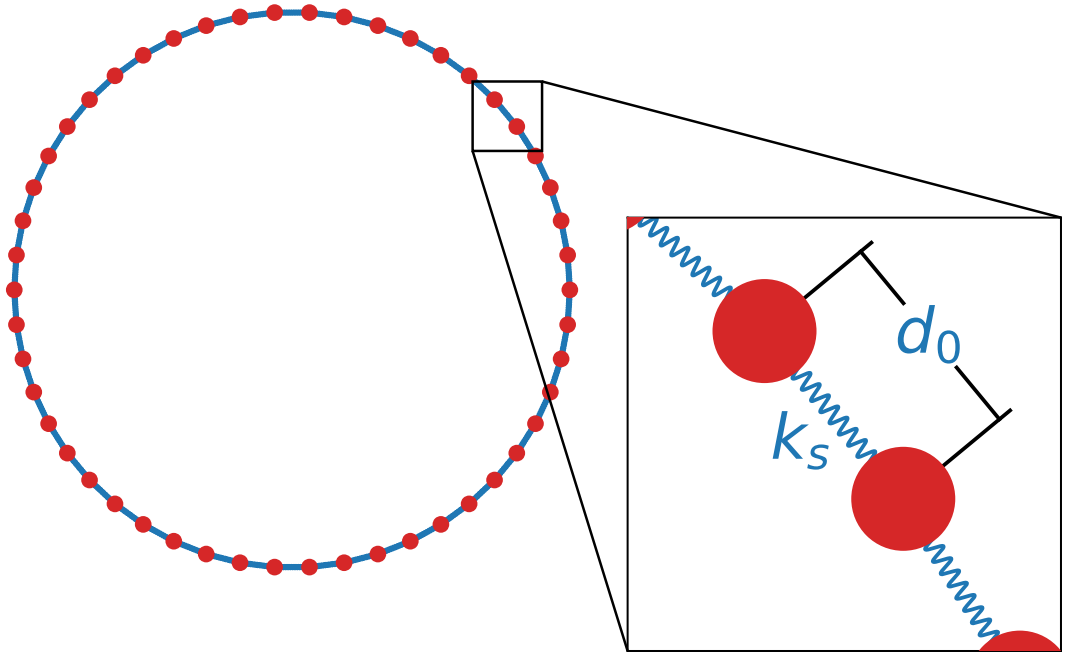

Figure 3 – Sketch of a cell composed of 50 particles connected by springs. The framed area represents an enlarged region, highlighting the springs that form the connections. In the enlarged region, the equilibrium distance and stiffness of the springs are also marked.

3.1.2 Bending Interaction

The bending interaction was introduced in the multi-particle model by Teixeira, Fernandes e Brunnet (2021). This interaction is responsible for maintaining the circular structure of the cell, minimizing the relative angle between pairs of particles that compose the membrane. In Equation 3.3, we have the potential that describes the bending interaction, denoted as U_b,

$$U_b = \frac{k_b}{2}\left(N - \sum_{i=1}^{N} \cos\left(\theta_{i,i+1} - \theta_0\right)\right) \tag{3.3}$$

where k_b is the potential constant, $\theta(i,j)$ is the relative angle between particle pairs $i, i+1$ and $j, j+1$, and θ_0 is the equilibrium angle. This potential can be interpreted as a kind of angular spring that changes the relative angle between particles, aiming to achieve an angle equal to θ_0. We define $\theta_0 = 0$ so that a free cell will tend towards a circular shape, even in this limit, it will be under tension.

In Figure 4, we have a sketch describing how the bending interaction acts on the membrane. Initially, the relative angle between two pairs of particles is determined and subsequently minimized.

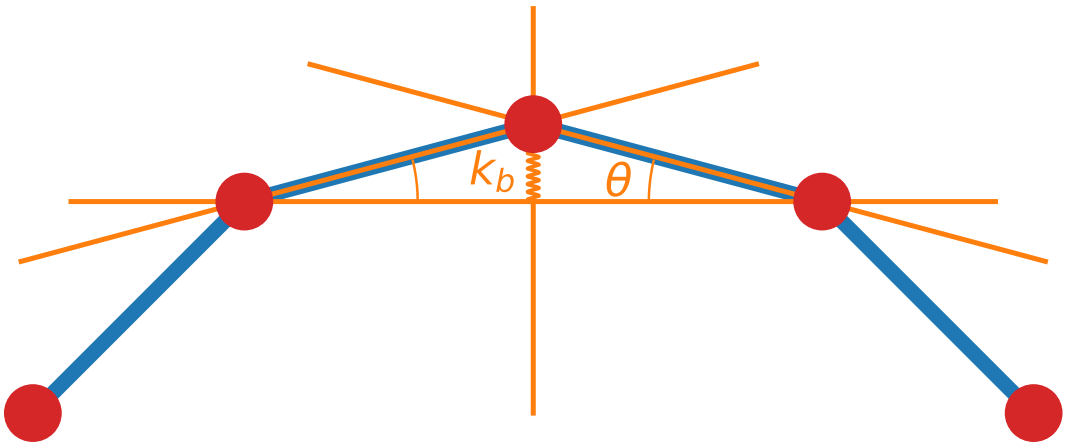

Figure 4 – Sketch of part of a cell. In orange, we can see the vectors connecting two pairs of particles and the angle formed between them. The bending potential tends to minimize this angle during the evolution.

3.1.3 Contact Interaction

The contact interaction is responsible for preventing a particle from passing through other particles in the membrane that are not its nearest neighbors. Teixeira, Fernandes e Brunnet (2021) used a Weeks–Chandler–Anderson potential to describe this contact interaction, which acts as a volume exclusion potential. In this work, we employ a simpler and more stable approach. The contact interaction is achieved through a repulsive force, $\vec{F}_c$, which decays linearly with distance, as presented by Szabó et al. (2006), with its maximum exactly on top of the particle and its cutoff point at a distance equal to d_e, as shown in Equation 3.4,

$$\vec{F}_c(i,j) = k_c \hat{d}_{i,j} \begin{cases} \left(1 - \frac{|\vec{d}_{i,j}|}{d_e}\right), & |\vec{d}_{i,j}| < d_e \\ 0, & |\vec{d}_{i,j}| \geq d_e \end{cases} \tag{3.4}$$

where k_c is the maximum amplitude of the repulsive force, and the indices i and j represent the interacting particles. It is important to note that, unlike the Weeks–Chandler–Anderson potential, this force does not result in an infinite repulsion at its center, giving our particles a "soft" character.

In Figure 5, we depict a sketch of a membrane composed of 30 particles compressed along a given direction. In this figure, the orange region represents where the contact interaction is active, preventing the membrane particles from touching each other even when compressed. We have marked a black circle on only one particle of the membrane to facilitate the visualization of the particles on which the contact interaction is acting. We

set the value $d_e = d_0$, ensuring that the repulsion experienced at the exact center between two other membrane particles is equal to the repulsion at the center of a single particle.

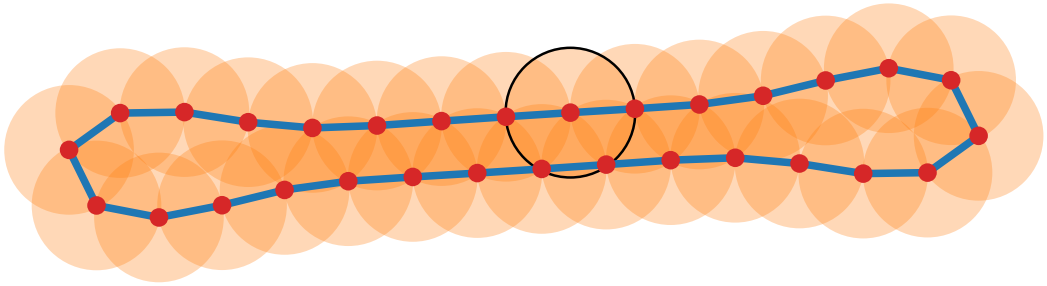

Figure 5 – Sketch of a cell composed of 30 connected particles being compressed. In red, we have the particles comprising the body, and in blue, their respective connections. In semi-transparent orange, we have marked the area of the repulsive force's reach. For better visualization, we have included a black circle on one of the membrane particles, indicating the boundaries of the contact interaction region.

3.1.4 Area Conservation

A good approximation in describing a cell, given the incompressibility of water, is to maintain constant volume. In two dimensions, this corresponds to conserving area. To introduce area conservation, we create a harmonic potential, U_A, which is minimized when the area of our cell, denoted as A, is equal to an equilibrium area, A_0,

$$U_A = \frac{k_A}{2}(A - A_0)^2 \,, \tag{3.5}$$

where k_A is the amplitude of this potential. The outcome of this potential is a force that always acts perpendicular to the membrane's surface, functioning as an internal pressure. If the area of our cell is larger than the equilibrium area, this force will point towards the inside of the cell.

As it acts as an internal pressure, the force stemming from this potential is crucial for reproducing experiments in which the cell undergoes some form of compression. In Figure 6, we present two cells, one on the left with an area above the equilibrium area, and one on the right with an area below the equilibrium area. In this figure, we have a grayed-out cell equivalent to the equilibrium area, along with vectors associated with the force resulting from the potential presented in Equation 3.5.

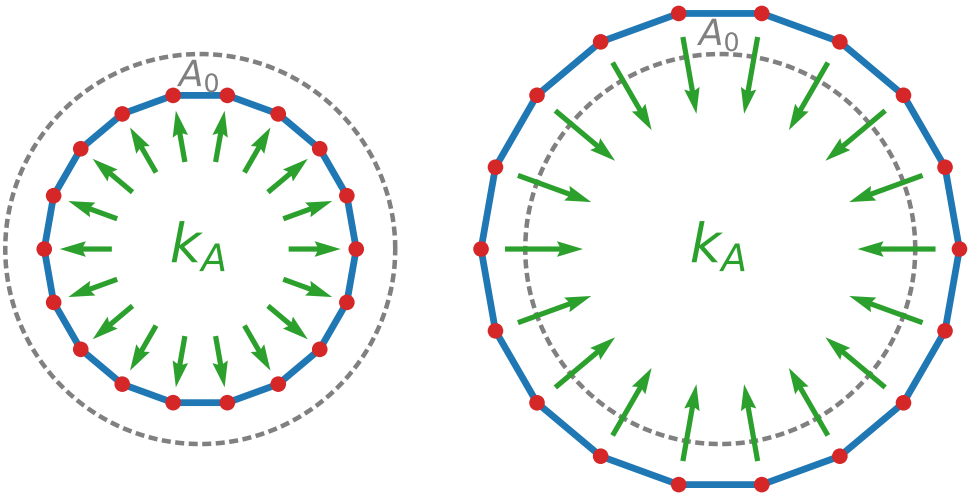

Figure 6 – Sketch of two cells composed of 18 particles each. In gray, there is a circle with an area equal to A_0, and in green, there are the force vectors resulting from area conservation. On the left, the body has an area smaller than A_0, causing the force vectors to expand the body. On the right, we have the opposite case, where the body's area is larger than A_0, causing the force to compress the body.

3.2 Cell Aggregate

The model used to represent a cell aggregate can be considered an extension of the single-cell model, where we include short-range adhesion and contact repulsion between particles of different cells (SZABÓ et al., 2006). This adhesion and repulsion are described by the force $\vec{F}_i(i,j)$, as presented in Equation 3.6.

$$\vec{F}_i(i,j) = \hat{d}_{i,j} \begin{cases} k_r \left(1 - \frac{|\vec{d}_{i,j}|}{d_r}\right), & |\vec{d}_{i,j}| < d_r \\ k_a \left(\frac{d_r - |\vec{d}_{i,j}|}{d_l - d_r}\right), & d_r \leq |\vec{d}_{i,j}| < d_l \\ 0, & |\vec{d}_{i,j}| \geq d_l \end{cases} \tag{3.6}$$

where i and j are indices of two distinct membrane particles, k_r is the maximum amplitude of the repulsion force, d_r is the equilibrium point between contact repulsion and adhesion force, k_a is the maximum amplitude of adhesion, and d_l is the cutoff point of the adhesion force.

It is interesting to note that the maximum adhesion of this force occurs in the region closest to the cutoff point, and the maximum repulsion occurs when the distance between two particles is zero. This structure creates a zone between the repulsive and attractive regions where particles can move freely.

In Figure 7, we have an example of a cell aggregate composed of 20 cells, each consisting of 50 particles. The red region represents where the repulsive force acts, while the green region represents where the adhesion force acts.

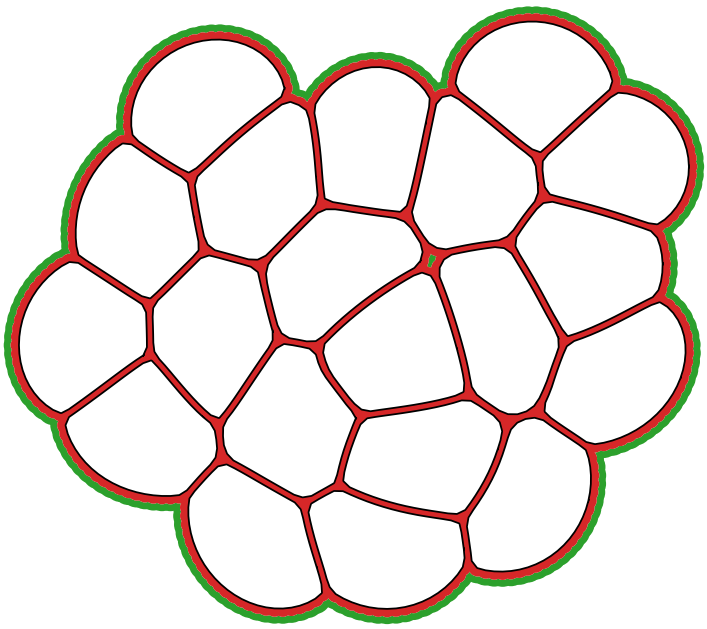

Figure 7 – A simulated cell aggregate with 20 cells, each composed of 50 particles. The red region represents the region of repulsion between the cells, while the green region represents the region of adhesion.

It's worth noting that, as described earlier, since the area between the adhesion force and the repulsion force is a region of free movement, the most energetically favorable configuration for the particles happens when the maximum number of particles occupies this region.

3.3 Wall Interaction

The walls in our model are composed of a large number of small repulsive particles positioned in such a way that the membrane particles are unable to pass through them. The repulsive force arising from the wall particles, denoted as F_w, is very similar to the contact interaction presented in Equation 3.4, as shown in Equation 3.7

$$\vec{F}_w(i,j) = k_w \hat{d}_{i,j} \begin{cases} \left(1 - \frac{|\vec{d}_{i,w}|}{d_w}\right), & |\vec{d}_{i,w}| < d_w \\ 0, & |\vec{d}_{i,w}| \geq d_w \end{cases} \tag{3.7}$$

where k_w is the maximum amplitude of the repulsive force, i is the index of a particle from a membrane, w is the index of a wall particle, and d_w is the cutoff point of the repulsive

force. In Figure 8, we have an example of a micropipette formed by several closely spaced particles.

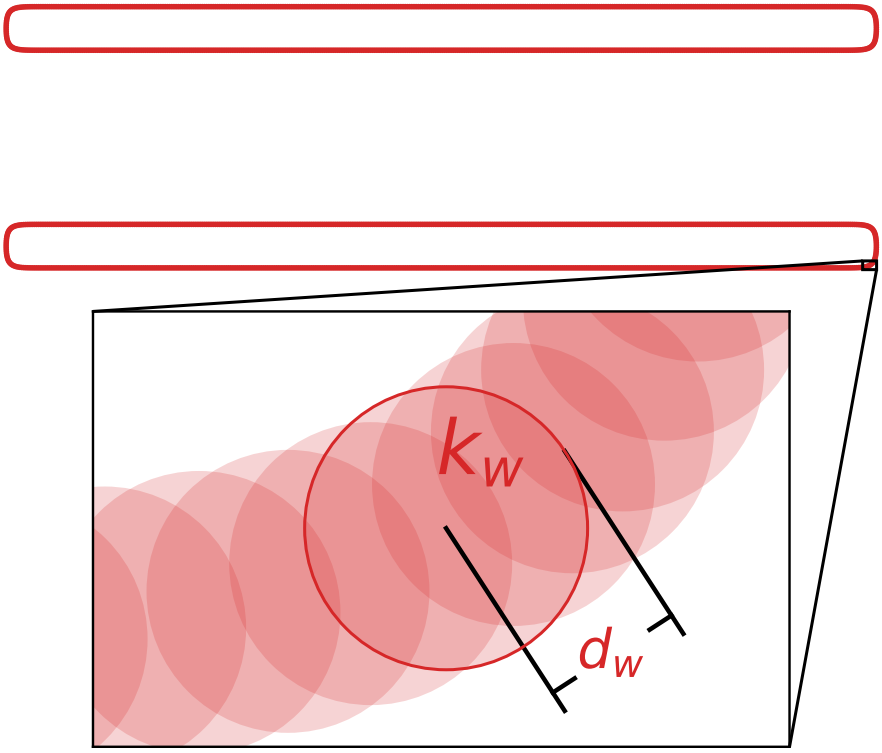

Figure 8 – Sketch of a micropipette composed of several particles with short-range repulsive interactions. The red regions highlight the interaction area of each particle. Due to the overlap of these interaction areas, the membrane particles are unable to pass through the wall particles.

To ensure that the membrane particles cannot penetrate the walls, the distance between the wall particles is set to $d_w/2$.

3.4 Dynamics

In the simulations, we use the same dynamics proposed by Teixeira, Fernandes e Brunnet (2021). The membrane consists of active Brownian particles that orient themselves according to the resultant force acting on them. The equations of motion for this dynamics follow the Langevin dynamics, which can be seen in Equations 3.9 and 3.8.

$$\frac{d\theta_i(t)}{dt} = \frac{1}{\tau}\arcsin\left(\left(\vec{n}_i(t)\times\frac{\vec{v}_i(t)}{|\vec{v}_i(t)|}\right)\cdot\vec{e}_z\right)+\xi_i(t) \tag{3.8}$$

$$\frac{d\vec{r}_i(t)}{dt} = v_0\vec{n}_i(t)+\mu\vec{F}_i(t) \tag{3.9}$$

In Equation 3.8, θ_i is the orientation of particle with index i, τ is defined as the relaxation time, $\vec{n}_i = (\cos(\theta), \sin(\theta))$, $\vec{v}_i$ is the velocity of the particle, $\vec{e}_z$ is a positive unit vector pointing in the z direction, and ξ_i is white noise with zero mean and a standard deviation of $\sqrt{2D_R}$. D_R is the angular noise coefficient, which is the inverse of the residence time, τ_r. In this particular work, we use $\tau_r = 100\tau$.

In Equation 3.9, the vector $\vec{r}_i$ gives us the position of particle with index i, v_0 is the self-propulsion velocity arising from activity, μ is the mobility, and $\vec{F}_i$ is the resultant force on the particle.

For the cell aggregate simulations, since the timescale of the motion associated with this activity is negligible compared to the motion associated with aspiration, i.e., $\mu\Delta P \gg v_0/R_c$, we can neglect the activity of membrane particles. Thus, our equations of motion are written as:

$$\frac{d\vec{r}_i(t)}{dt} = \mu\vec{F}_i(t)\ . \tag{3.10}$$

4 Simulation

This work focuses on two distinct types of simulations: single cells and cell aggregates. Single-cell simulations are conducted with membranes composed of up to 500 particles. In contrast, simulations of cell aggregates are performed with simplified membranes, containing only 50 particles each. Each cell aggregate simulation is carried out with 500 cells, totaling $25,000$ particles in the system.

4.1 Single Cell Simulation

As mentioned earlier, single-cell simulations are conducted with membranes composed of a variable number of particles ranging from 250 to 500. For illustrative purposes, the figures presented in this section will depict membranes composed of 500 particles.

The initial condition of the simulation is prepared with a perfectly circular cell with a radius of R_c. A micropipette is included in the system with an opening equal to $2R_p = R_c/2$, which is one-quarter of the cell's radius. The cell is positioned in contact with the micropipette, and then an aspiration pressure ΔP is initiated. The pressure is represented by a force that acts on each membrane particle that is inside the micropipette and is not in contact with the inner walls of the micropipette. Similar to the force arising from area conservation, the force associated with pressure is constructed to be perpendicular to the membrane's surface, and its magnitude is designed so that the relationship between force and pressure results in a pressure equal to ΔP. The length of the membrane region within the pipette, the deformation length, is defined as L_p.

After some time of aspiration, the elastic forces of the cell membrane reach equilibrium with the aspiration pressure, leading the cell to a steady-state regime, except for its internal activity. In Figure 9, we have an example of a cell already aspirated by a micropipette. In this figure, we also have the initial configuration of the cell shown in gray.

4.2 Cell Agreggate Simulation

Our initial condition is established using 500 cells, each composed of 50 particles. These cells are randomly positioned within a circular region under extreme compression, with each cell occupying only a quarter of its equilibrium area. Subsequently, the cells evolve in the absence of external forces until they reach their equilibrium volume. On the left side of Figure 10, an example of cells randomly positioned under extreme compression is presented, while on the right side of the same figure, the final state is depicted, attained

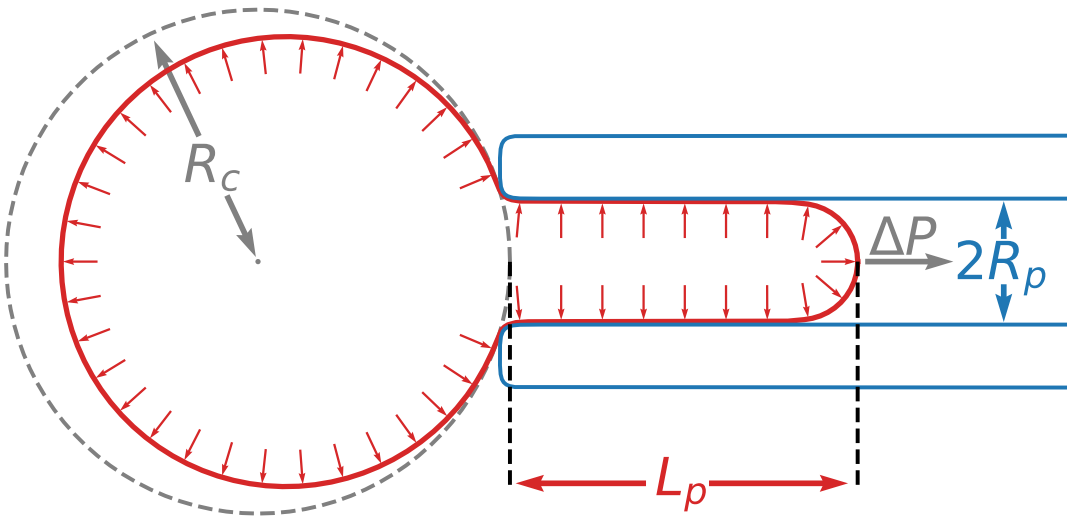

Figure 9 – An example of a simulation of a cell being aspirated by a micropipette. In gray, we have the sketch of the initial configuration of the cell, and in red, we have the equilibrium configuration after aspiration. In the figure, we highlight the definitions of the cell radius, R_c, micropipette opening, $2R_p$, aspiration pressure, ΔP, and deformation length, L_p.

after the system reaches equilibrium. The radius of the cell aggregate, R_A, can be estimated

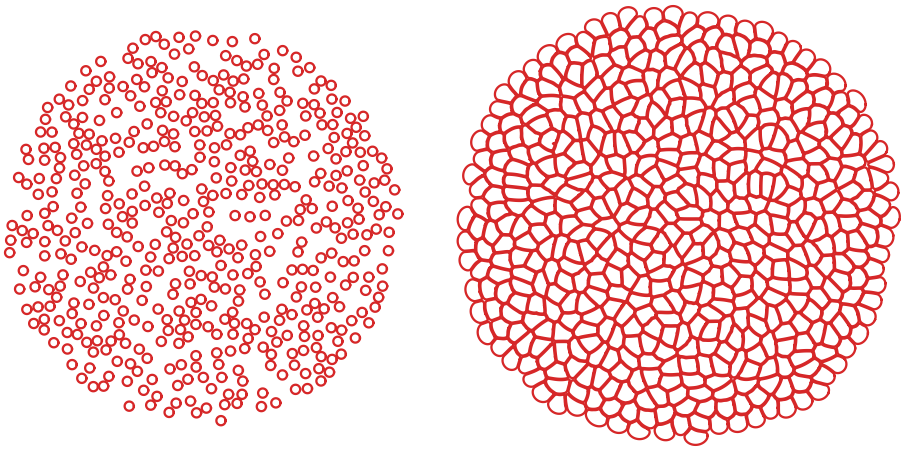

Figure 10 – Arrangement of cells to generate the initial condition of a cell aggregate. Initially, the cells are randomly positioned along a circle in a state of extreme compression, as shown on the left. After the cells are positioned, the system evolves until the cells reach their equilibrium volume, as shown on the right.

from the relationship between the area of an individual cell and the total area of the

aggregate, following the equation:

$$R_A = \sqrt{(N^c)} R_c \ , \tag{4.1}$$

where N^c is the number of cells in the system.

A micropipette with an opening of $2R_p = 10R_c$ is inserted into the system. This opening was defined so that at most 5 perfectly circular cells can pass through the micropipette opening simultaneously. If the observed behavior in the simulations exceeds 5, it provides clear evidence of cellular deformation.

With the micropipette in the system, we position the cell aggregate against the micropipette and initiate pressure in the region outside the micropipette. This pressure, acting on all the cells located in the external region of the aggregate, forces the aggregate into the micropipette. An example of this situation can be seen in Figure 11.

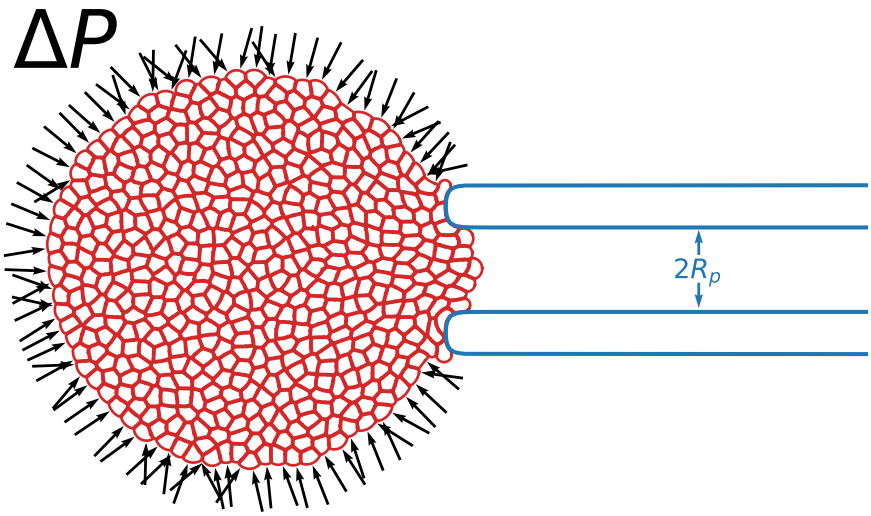

Figure 11 – Cell aggregate under pressure positioned in contact with the micropipette. The black vectors highlight the orientation of the pressure force applied to the aggregate.

Throughout the evolution, it is possible to measure the deformation length of the aggregate as it enters the micropipette. In Figure 12, we have the same system as shown in Figure 11 after some time of evolution, where we can clearly see the displacement of the cells and the deformation length.

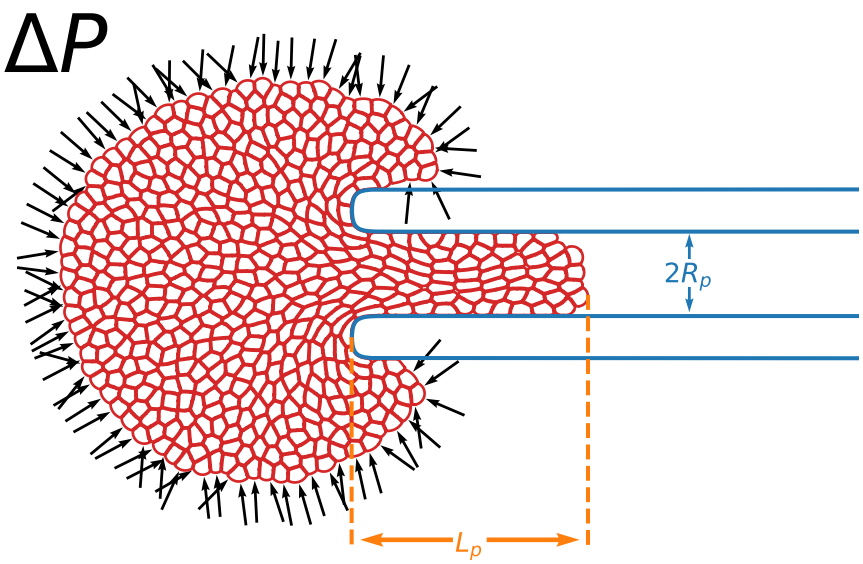

Figure 12 – Cell aggregate under pressure positioned in contact with the micropipette after some time of evolution. Highlighted in orange is the deformation length.

4.3 Program

The simulations were conducted using a program developed during this study. This program comprises two primary components: a main Fortran95 program optimized for enhanced performance, and a Python script responsible for configuring the simulation setup and invoking the Fortran95 program. Further details about the implementation can be found at <https://github.com/ourique-gus/micropipette_aggregate>.

5 Results

In this chapter, we will highlight the results obtained from the conducted simulations. To facilitate future comparisons, we have nondimensionalized the system variables by defining all quantities based on the parameters μ, τ, and R_c.

5.1 Single Cell

For single-cell simulations, we sought to assess the impacts of the area parameter (k_A), the bending parameter (k_b), the self-velocity (v_0), and the spring constant (k_s) on the system's evolution. We conclude this part by comparing the values of an effective spring constant resulting from an approximate series association and the simulations.

5.1.1 Compressibility

Taking into account that the main difference between the model proposed in this work and the model presented by Teixeira, Fernandes e Brunnet (2021) is the area conservation, we initially conducted simulations by varying the parameter k_A. The parameters for these simulations are $N = 500$, ΔP=$7.5\,(\tau\mu)^{-1}$, k_b=$10^{-8}\,R_c^2/(\tau\mu)$, k_s=$10\,(\tau\mu)^{-1}$, and v_0=$5 \times 10^{-6}\,R_c/\tau$. With these parameters fixed, we varied the value of k_A over five orders of magnitude, from $10^{-3}\,(\tau\mu R_c^2)^{-1}$ to $10^2\,(\tau\mu R_c^2)$.

To facilitate the analysis of the results, we defined parameter k_A^0=$10^4\,(\tau\mu R_c^2)$. Throughout the simulations, we observed that the variation of volume scales very slightly with the variation of k_A, leading us to define the quantity $\log(k_A/k_A^0)$, which is dimensionless and, due to base-10 logarithm, facilitates the visualization of the influence of k_A.

In Figure 13, we present the relative volume of a cell during the system evolution, absorbed for various values of $\log(k_A/k_A^0)$. It can be observed that for values above -3, the cell volume remains nearly constant. Between -6 and -3, there is a cell area variation of less than 8 percent compared to the area of a circular cell. However, for values below -6, the cell is completely absorbed, indicating that area conservation plays a fundamental role in simulating micropipette aspiration. This sets boundaries on parameter k_A because the experiment aims to establish a relationship between the membrane extension inside the micropipette, L_p, and the applied pressure difference, ΔP, in the cell. Specifically, it is supposed that the length of the cell membrane inside the micropipette is significantly smaller than the entire cell perimeter.

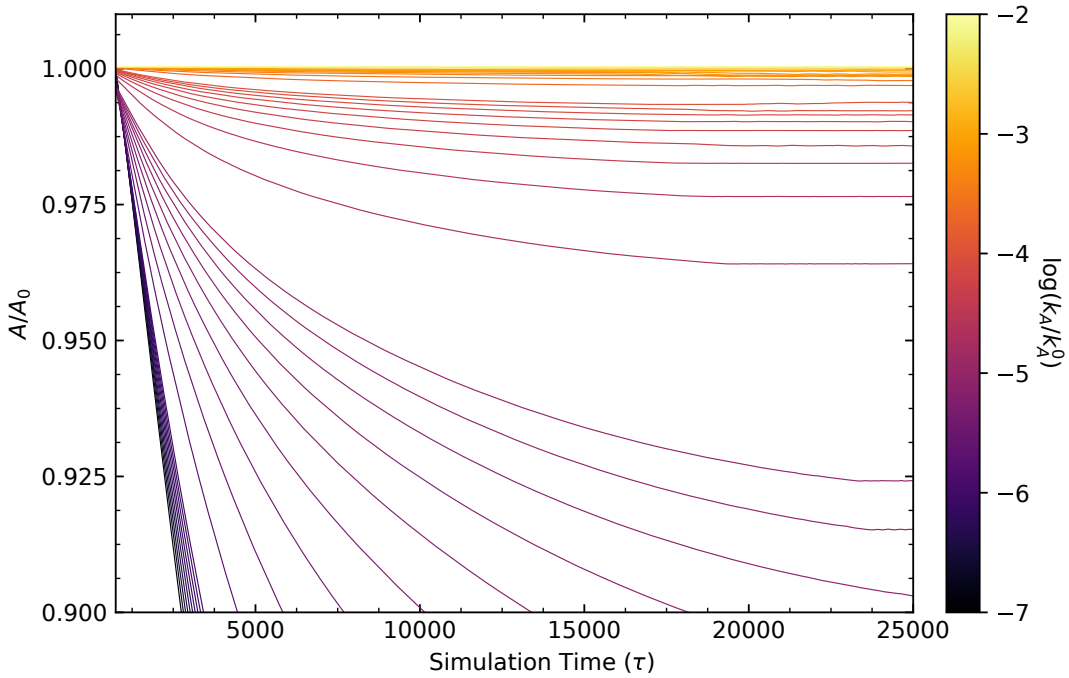

Figure 13 – The relative volume of a cell throughout its evolution while being aspirated by a micropipette is shown. For $\log(k_A/k_A^0)$ values greater than -3, the cell volume remains nearly constant. For $\log(k_A/k_A^0)$ values greater than -6 and less than -3, the relative volume is above 0.92. However, for $\log(k_A/k_A^0)$ values less than -6, the cell is completely absorbed.

5.1.2 Bending Rigidity

To investigate suitable values for the bending potential in our simulations, we varied the value of the constant, k_b, from $10^{-9}\, R_c^2/(\tau\mu)$ to $10^{-2}\, R_c^2/(\tau\mu)$, while keeping the other constants as used previously in the determination of k_A, and maintaining $k_A{=}10^2\,(\tau\mu R_c^2)^{-1}$. To facilitate data interpretation, we defined $k_b^0{=}R_c^2$, allowing us to define the quantity $\log(k_b/k_b^0)$, which is useful for comparing the differences in our simulations across a wide parameter range.

In Figure 14, we present the deformation length of the cell for different values of k_b. We notice that no significant differences occur, and the small variations do not show any correlation with the value of k_b.

5.1.3 Activity and Relaxation Time

To investigate the relevant parameter range for activity in the system, we initially defined the auxiliary parameter $v_0^0{=}10^{-2}, R_c/\tau$ and kept the other parameters at the same values mentioned earlier. Thus, we defined $\log(v_0/v_0^0)$, a parameter that we varied from -9 to -2.3.

Observing Figure 15, we notice three distinct regimes: The first regime occurs

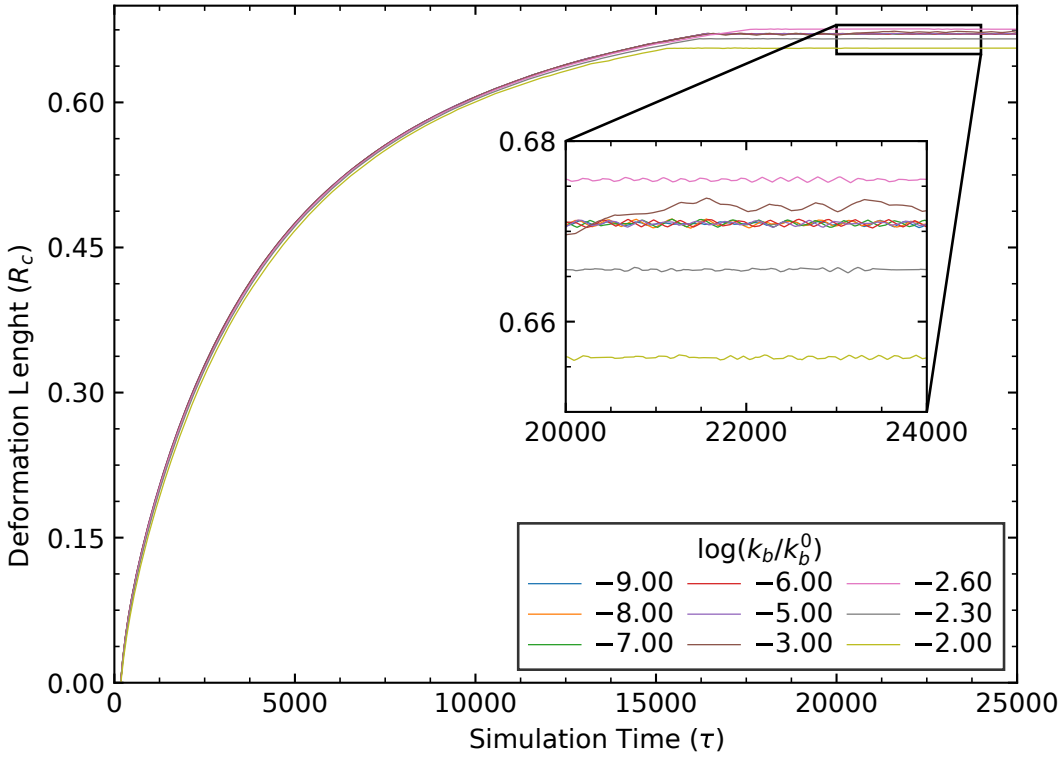

Figure 14 – Deformation length of the cell being aspirated for various values of $\log(k_b/k_b^0)$. The zoomed-in region highlights that the variation in deformation length is very small and does not follow any pattern associated with the value of k_b.

when $\log(v_0/v_0^0) < -3.2$, where the membrane is absorbed by the micropipette and reaches a steady state. In this regime, we perceive that the role of activity is to accelerate the aspiration process. The second regime occurs when $-3.2 \leq \log(v_0/v_0^0) < -2.9$, where the membrane quickly reaches its maximum extension due to the high activity of membrane particles. However, because of this high activity, considerable fluctuations occur around an equilibrium point. The third regime, which occurs when $\log(v_0/v_0^0) \geq -2.9$, shows that the activity is so high that the cell's deformation length quickly passes its equilibrium point. However, in this case, the oscillations due to high activity are not stable, forcing the polarization of membrane particles to align along the membrane's direction. In this case, the cell starts rotating, as described by Teixeira, Fernandes e Brunnet (2021).

5.1.4 Elasticity

The effective elastic constant, k_{eff}, resulting from the series association of identical springs with equilibrium length d_0, turns out to be the constant of each spring divided by the number of springs, $k_{\text{eff}} = k_s/N$. If we want to vary the number of springs while keeping k_{eff} and the equilibrium length of the association $L = Nd_0$, we can define ρ_s, so that,

$$k_{\text{eff}} = \frac{k_s}{N} = \frac{k_s d_0}{N d_0} = \frac{\rho_s}{L} \tag{5.1}$$

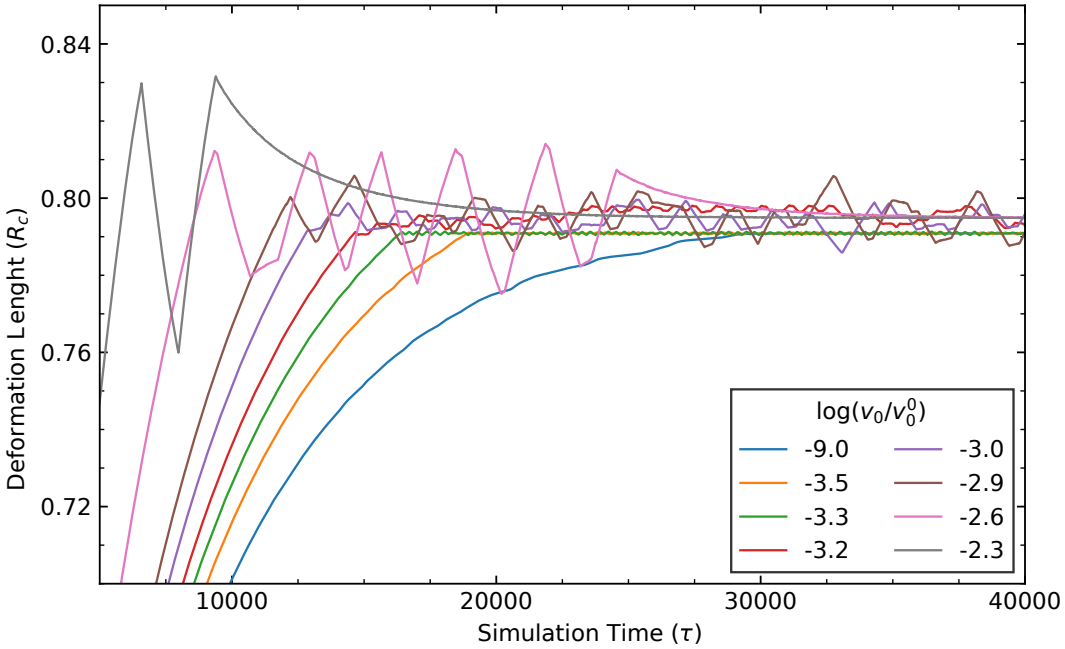

Figure 15 – Deformation length of the cell being aspirated for various values of $\log(v_0/v_0^0)$. We can see three distinct regimes in this figure: one where $\log(v_0/v_0^0) < -3.2$, in which the membrane reaches its maximum deformation length and enters a state of equilibrium with small fluctuations; one where $-3.2 \leq \log(v_0/v_0^0) < -2.9$, in which the membrane reaches equilibrium with very high fluctuations due to the high activity; and finally, one where $\log(v_0/v_0^0) \geq -2.9$, in which the membrane has such high activity that the most favorable configuration to dissipate internal energy is rotation.

The quantity ρ_s associates the spring constant of the springs constituting the membrane and their equilibrium distance. To maintain parameters L and k_{eff} constants, when we increase the number of particles composing a membrane, the equilibrium distance between the springs must decrease. This property ensures that ρ_s is a valid measure for both discrete systems with a finite number of connected springs and continuous systems, where the distance between particles would be infinitesimal.

Starting from the equilibrium system after aspiration, we can calculate the value of ρ_s using the balance between the aspiration force associated with pressure and the deformation in the cell perimeter,

$$\rho_s = \frac{2\pi R_c R_p \Delta P}{l' - l} \,, \tag{5.2}$$

where l and l' are, respectively, the cell perimeter before and after aspiration.

It is interesting to note that, if we use a similar approach to that proposed by Theret et al. (1988), assuming that the cell perimeter is much larger than the deformation length, we can make the approximation $(l' - l) \simeq 2L_p$, as shown in equation 5.3.

$$\rho_s = \frac{\pi R_c R_p \Delta P}{L_p} \tag{5.3}$$

Equation 5.3 is more convenient for comparison with experimental data because it only requires measuring the deformation length.

To validate our simulations, we compared our measured value of ρ_s with the data generated by simulations, which we denote as ρ_s^f, for various values of aspiration pressure, with the input value of ρ_s defined as ρ_s^i. To perform this comparison, a graph was plotted between the quantities $R_p\Delta P$ and $(l'-l)/(2\pi R_c)$ resulting from our simulations for various values of ρ_s^i. Knowing that the slope of this relationship is given by ρ_s^f, we used a linear fit to recover this value and compared it with the input value used in the simulation.

In Figure 16, we present simulations conducted with various distinct aspiration pressures for five different values of ρ_s^i, represented by different colors. The lines in this figure represent the linear fits. In the legends, we provide the input value for ρ_s, ρ_s^i, and the value obtained through linear fitting, ρ_s^f.

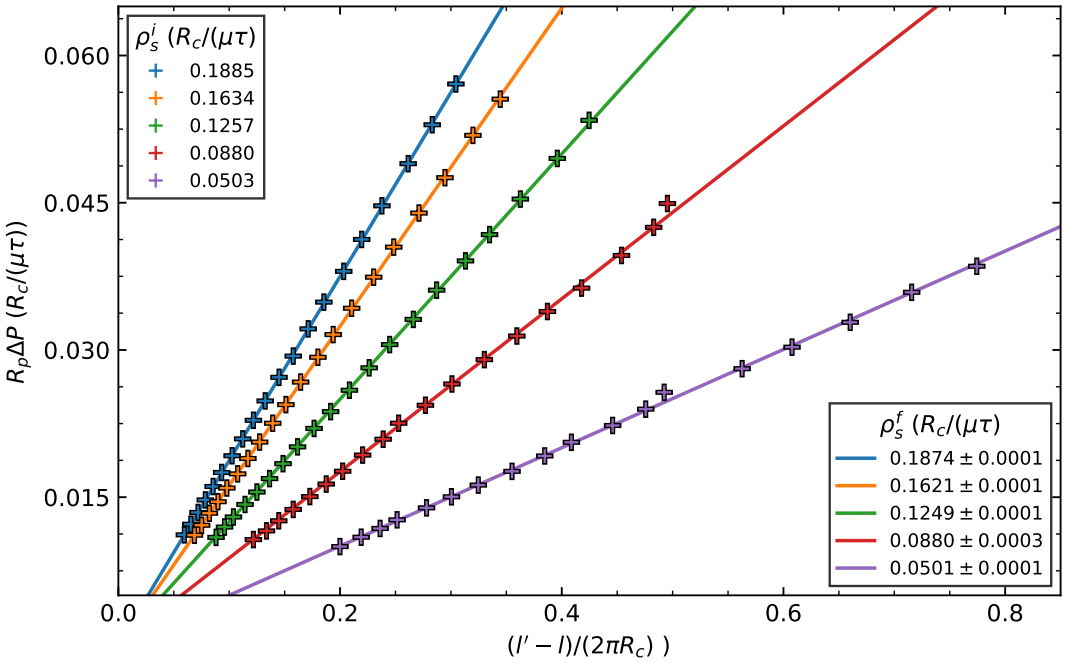

Figure 16 – Values of $R_p\Delta P$ as a function of $(l'-l)/(2\pi R_c)$, obtained from our simulations. The colors indicate different input values of ρ_s, denoted as ρ_s^i, while the lines represent the result of the linear fit, from which we determined the value of ρ_s^f for comparison. The legends provide the values of ρ_s^i and ρ_s^f.

5.2 Cell Aggregate

For cellular aggregates, the studies were centered on measuring the effect of microscopic quantities on their viscoelastic-plastic properties. To simplify our analysis, we define the parameter τ as an arbitrary simulation time scale. To streamline the analysis, certain parameters were predefined for all subsequent simulations, and these parameters include k_b=0.25 $R_c^2/(\tau\mu)$, k_s=200 $(\tau\mu)^{-1}$, k_c=1 $(\tau\mu)^{-1}$, k_A=300 $(\tau\mu R_c^2)$, k_r=100$(\tau\mu)^{-1}$ and ΔP=2.0 $(\tau\mu)^{-1}$.

5.2.1 Cell-to-Cell Adhesion

To determine the influence of cell adhesion, we varied the value of k_a from 0.0 $(\tau\mu)^{-1}$ to 1.0 $(\tau\mu)^{-1}$, thus conducting simulations in which the aggregate cells are drawn into the micropipette for each set of parameters. It is important to note that for $k_a = 0.0\,(\tau\mu)^{-1}$, our system represents cells with no intercellular adhesion. In Figure 17, we can observe the evolution of deformation length as a function of time for various cell adhesion values.

In this figure, we can link the initial progression to a purely elastic behavior that eventually transitions into a steady flow, except in the case of strong cell adhesion that blocks the flow. It's worth highlighting that Equation 2.18 generically captures and may be used to describe this outcome.

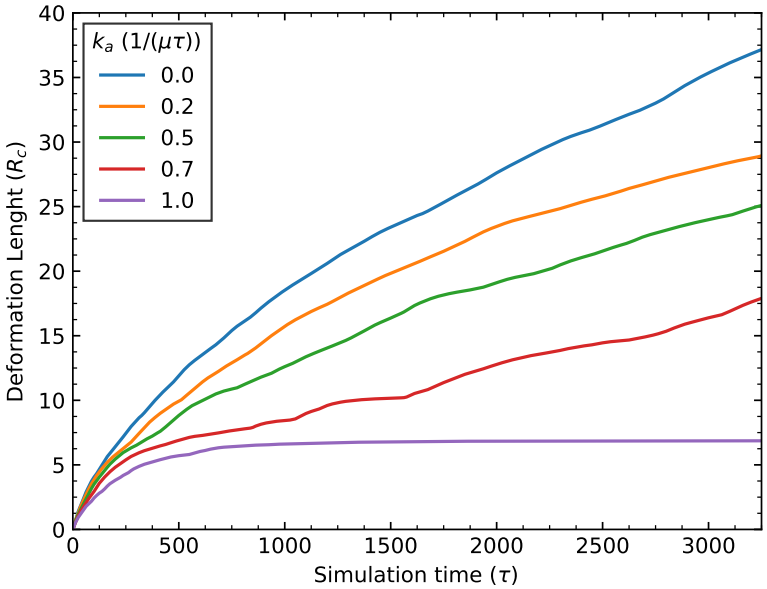

Figure 17 – Evolution of deformation length for cell aggregations under micropipette aspiration simulation. Each color indicates a different cell adhesion, k_a, parameter adapted for the simulation. For clarity, only curves with five different values of k_a are shown in this graph.

In order to match the simulation outcomes with the rheological model adopted,

simplification is essential to remove parameter overlaps. Thus, we rewrite Equation 2.18 in the form:

$$\varepsilon = At + B\left(1 - e^{-\frac{t}{C}}\right) \tag{5.4}$$

being $A = \frac{\sigma - \sigma_Y}{\eta_Y}$, $B = \frac{\sigma}{G_{\text{cortex}}}$ and $C = \tau_c$.

In this context, parameter A defines the velocity of the plastic flow, parameter B indicates the maximum elastic deformation of the aggregate, and parameter C involves the characteristic timescale of the elastic deformation.

Figure 18 presents the values of parameter A for various values of k_a. The gray region represents the range where the aggregate becomes purely elastic.

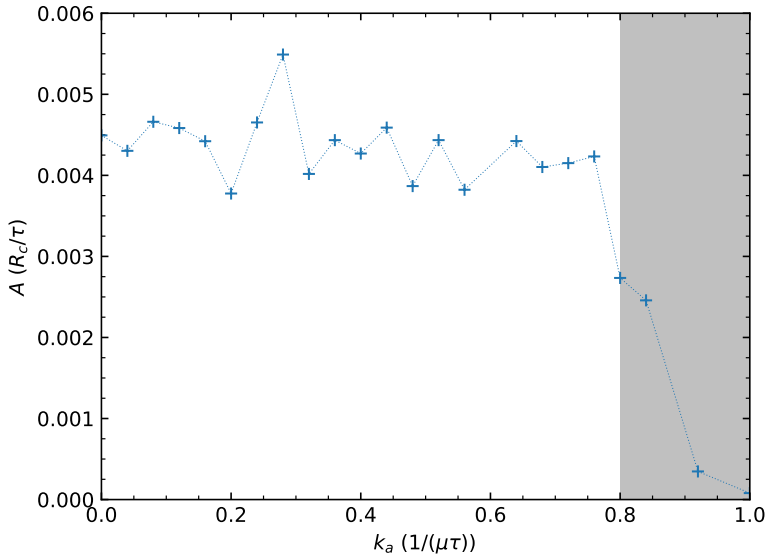

Figure 18 – Parameter A calculated for simulations with various values of k_a. The shaded region delineates the aggregate in a purely elastic state.

For $k_a < 0.8$, we did not find any clear relation between the adhesion strength and the flow speed, since all curves within this criteria tend asymptotically to the same slope. For higher values of k_a we can observe an abrupt state change where the aggregate becomes purely elastic with the flow stopping after a transient. We interpret this result as indicative that, for a fixed pressure difference, ΔP, fluid viscosity is independent of adhesion forces. This behavior is expected since cell adhesion in our model is represented by a purely elastic potential, not providing any friction-like contribution. However, when adhesion is significant enough to prevent neighbor exchange, the aggregate starts behaving like an elastic tissue.

For parameter B, as we can observe in Figure 19, we find that for cells with higher adhesion, the amplitude of elastic deformation is smaller. The results for this parameter indicate that cellular adhesion is intrinsically correlated with the elastic modulus of the

cells. This can be interpreted as the adhesion region surrounding the cell playing a role as an extension of its overall volume; however, with a "soft" function, allowing cells in contact to function as an extended body. In other words, cells with higher adhesion would be represented by interfaces that are less compliant, resulting in a shorter distance between cells within the aggregate.

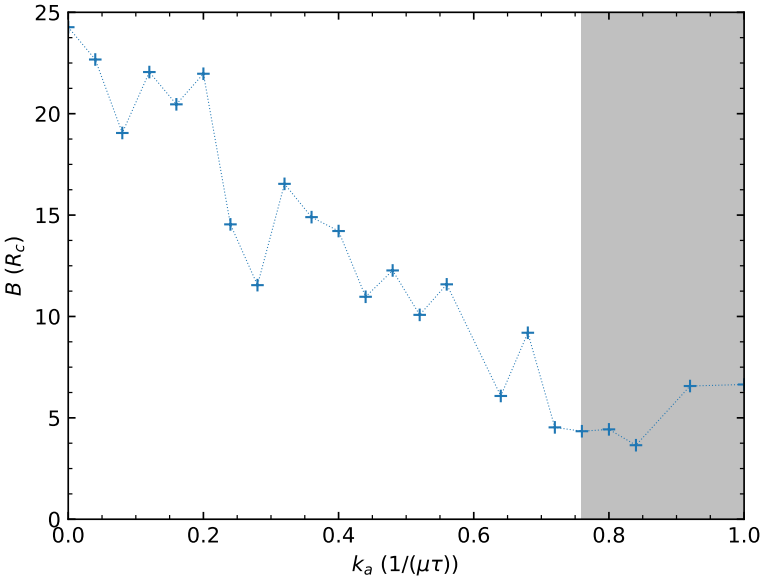

Figure 19 – Parameter B calculated for simulations with various values of k_a. The shaded region delineates the aggregate in a purely elastic state.

We also found, as shown in Figure 20, that the parameter C, responsible for categorizing the temporal scale of elastic deformations within the aggregate, exhibits low correlation with cellular adhesion in our model. Since our studies were limited to the visco-plastic region, it was not possible to establish precise correlations in regions where the aggregate is purely elastic.

It is noteworthy to mention that parameters A, B, and C predominantly characterize the macroscopic viscoelastic-plastic properties of our system, rendering them suitable for describing cellular aggregates in experimental scenarios.

5.2.2 Aggregate Elasticity

To investigate the elastic properties of aggregates represented by our model, we conducted simulations with a fixed adhesion force, k_a, set at $0.5\,(\tau\mu)^{-1}$. The suction pressure, ΔP, was varied across a range of values from $0.0\,(\tau\mu)^{-1}$ to $2.0\,(\tau\mu)^{-1}$, as illustrated in Figure 21.

In this figure, we observe a clear linear relationship between the deformation length and the aspiration pressure at low pressures, as expected, since our membrane adhesion potential is purely elastic up to its breakdown. Between aspiration pressure

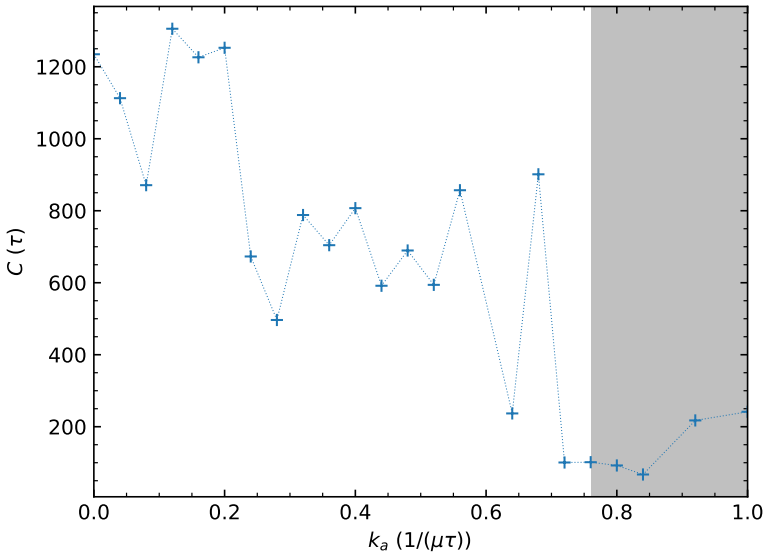

Figure 20 – The parameter C calculated for simulations with various values of k_a. The shaded region delineates the aggregate in a purely elastic state.

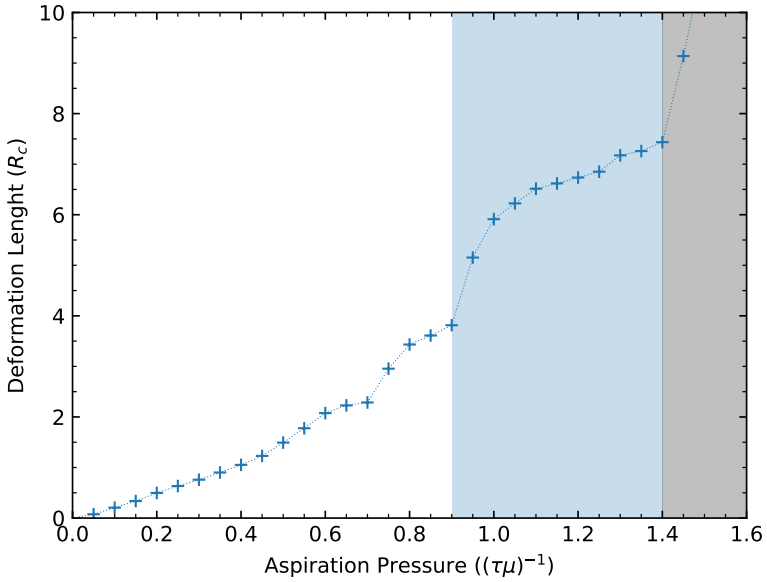

Figure 21 – Aggregate deformation length for several distinct aspiration pressure. The blue region indicated when the aggregate present small plastic deformations, but still on a elastic state. The gray region indicates the elastic rupture of the system, starting a visco-elastic-plastic flow.

ΔP=0.9 $(\tau\mu)^{-1}$ and ΔP=1.40 $(\tau\mu)^{-1}$, the deformation length response exhibits a non-linear behavior due to some plastic behavior inside the aggregate. For ΔP>1.4 $(\tau\mu)^{-1}$, the aspiration pressure is strong enough to break the membrane adhesion, leading the cell aggregate to a visco-elastic-plastic flow.

In a subsequent analysis, we varied cellular adhesion, k_a, from 0.1 $(\tau\mu)^{-1}$ to 0.5 $(\tau\mu)^{-1}$, as depicted in Figure 22. In this figure, we introduced a constant offset to the

aspiration length for better visualization, as our focus is on determining the aspiration pressure at which the aggregate becomes fully aspirated. For clarity, we will refer to this aspiration pressure limit as "breakdown pressure". As expected, we observe that aggregates composed of cells with higher adhesion require a greater aspiration pressure to be fully aspirated, transitioning from an elastic state to a visco-plastic state.

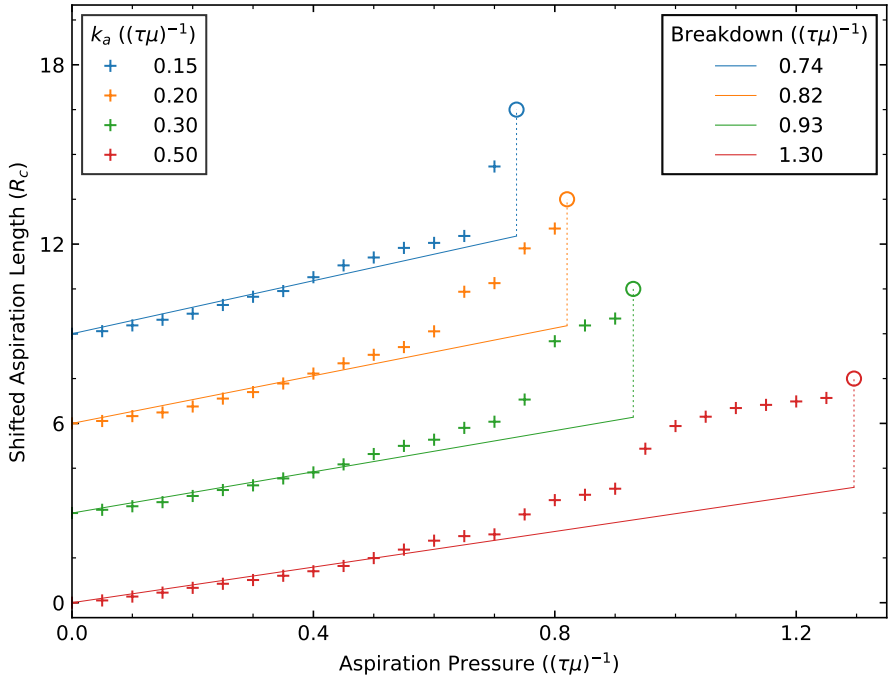

Figure 22 – Simulation of cellular aggregates with distinct cellular adhesion being aspirated while varying the aspiration pressure. In this figure, we can observe that beyond a certain threshold, the aspiration pressure breaks the adhesive bonds between the cells, causing the aggregate, previously elastic, to exhibit visco-plastic behavior. Note that for higher values of cellular adhesion, a greater aspiration pressure is required to disrupt the connections between the cells.

With this analysis, we can establish a relationship between the breakdown pressure and cellular adhesion, as illustrated in Figure 23. In this figure, the linear dependence of the breakdown pressure on the strength of adhesion force is evident. The transition from the elastic regime to the plastic one, where the aggregate flows into the pipette is certainly not a simple phenomena, but we may understand it in part from the model used, since the maximum adhesive force exerted by the particles on the cellular membrane linearly depends on the cellular adhesion constant.

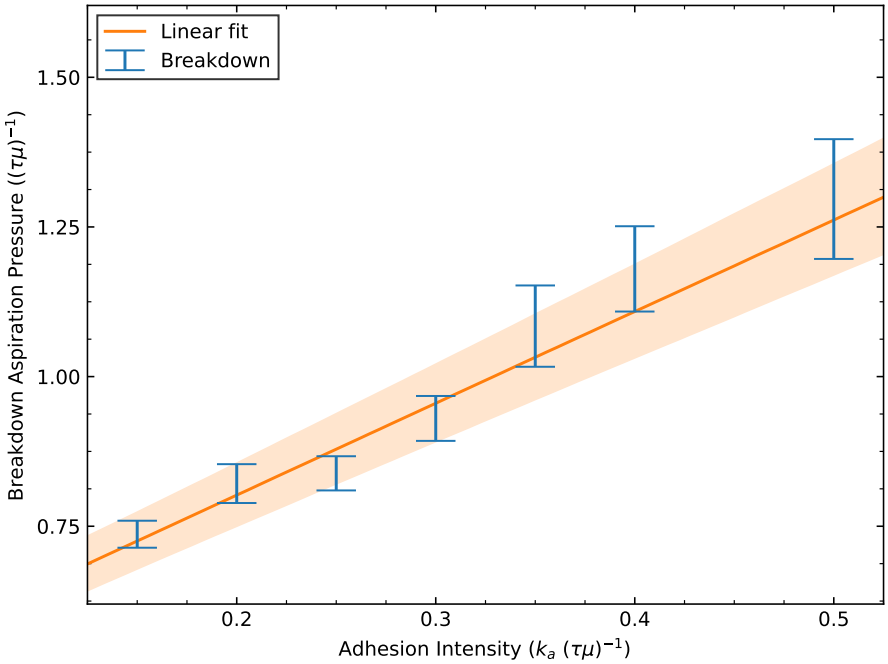

Figure 23 – Breakdown aspiration pressure as a function of cellular adhesion intensity, along with a linear fit. In this figure, it is apparent that the data is well-represented by a linear fit, consistent with the expectations of our model.

6 Conclusion

The simulations we develop in this thesis demonstrate the possibility of creating realistic representations of cells using a minimalist two-dimensional model. This opens up opportunities to explore additional parameters or more varied experimental conditions, such as aspiration through a micropipette.

Single cell simulations show that the conservation of area, the two-dimensional equivalent of volume, is essential for realistic simulations. Since water, which constitutes the majority of the cell's interior, is incompressible, it was expected that its conservation would play a dominant role. Conversely, we also observed that the bending potential plays no significant role. This is a direct consequence of the experiment to which the simulated cell was subjected. A circular cell under the influence of the bending potential is always under tension, as the equilibrium point is when the relative angle between particle pairs is zero (see Figure 4). During the micropipette aspiration experiment, the region of the membrane inside the micropipette walls is perfectly aligned, minimizing the bending potential and its contribution to the experiment as a whole.

We have also investigated the effect of particle activity. During the simulation, the orientation of active particle movement aligns with the force associated with aspiration pressure. This alignment between active movement and aspiration pressure results in an effective aspiration pressure that can stretch the cell beyond what the aspiration pressure alone would achieve. However, once reaching the limit of effective aspiration pressure, the membrane particles start aligning with other elastic forces in the system, causing the membrane to retract to a point where the aspiration pressure is capable of stretching the system. At this point, the activity of particles in the membrane reaches equilibrium, leading to membrane particles rotating along the membrane direction or adopting vibrational movements.

Starting from the equilibrium of forces, it was possible to define a clear relationship to determine the elastic properties of a single membrane composed of various particles connected with springs. The parameter used to define the elasticity of our system was $\rho_s = d_0 k_s$, a quantity valid for both discrete and continuous systems, interpretable as an elastic density. We compared the input value of ρ_s in our simulations with the measured value obtained from the simulation results and found that the difference between these values is below 1%, validating our simulations. This demonstrates that this method can be used to map microscopic properties from simulations and compare them with experimental data.

A potential extension of this cellular model involves a three-dimensional framework.

An unrealistic consequence of the two-dimensional model, as mentioned earlier, is rotation. This phenomenon is not commonly observed in real cells (TEIXEIRA; FERNANDES; BRUNNET, 2020) and results from the alignment interaction and from the reduction in the number of dimensions. The closed-ring structure facilitates system rotation, as particles can move in loops without resistance. In a three-dimensional system, this type of movement is less likely, resulting in more realistic cellular activity. Introducing a third dimension to the model could address the limitation of rotational behavior observed in the two-dimensional model. The closed-ring structure, which promotes rotation in two dimensions, may be constrained in a three-dimensional space, leading to cellular activities that align more closely with the observed behaviors in real cells. This modification may provide a more accurate representation of cellular dynamics, contributing to a better understanding of cell behavior in three-dimensional environments. Additionally, exploring the impact of dimensionality on cellular activities can offer insights into the fundamental differences and similarities between two-dimensional and three-dimensional cellular systems.

For cellular aggregates, our simulations indicate that the aggregate of cells composed by multiparticles can be accurately mapped to a rheological model containing intra-cellular viscoelasticity and inter-cellular plasticity. With this model, we can relate microscopic and macroscopic properties, such as the strength of adhesion force concerning deformation length in elastic regimes.

One intriguing observation pertains to the apparent lack of correlation between cellular adhesion and the speed of aspiration flow. Initially, we expected that cellular adhesion would function as an internal viscosity (Abbasi et al., 2021). However, our simulations revealed that adhesion plays no role in the internal viscosity, only in cell cohesion. This suggests that the overall viscosity of the system is predominantly governed by cellular mobility (μ), implicit in the basic overdamped dynamical equations. Nevertheless, in instances where adhesion surpasses the aspiration force, it effectively obstructs the entire flow. This inhibition prevents any meaningful exchange of neighboring cells, causing the aggregate to exhibit behavior analogous to that of an elastic tissue.

The obtained result, although atypical, aligns with expectations for our model. In Figure 7, distinct regions are apparent where membrane particles reach equilibrium, experiencing neither repulsive contact forces nor attractive adhesion forces with neighboring particles. Because this adhesion lacks any connection to neighbor exchanges or movement direction, it doesn't contribute to friction or viscosity. This characteristic allows cells to freely exchange neighbors. An extension to this model could involve introducing an adhesion term inversely related to the alignment between membrane particle positions and their movement velocities. Such a term could impede neighbor exchanges, taking on a role akin to viscosity.

The configuration in which the aggregate simulates the characteristics of an elastic

tissue holds significant relevance, particularly in the realm of medicine, where it can be analogized to an assembly of tumor cells. Outcomes from our simulations indicate that, under low pressures, the aggregate manifests a linear response to the applied aspiration pressure. As the pressure slightly increases, a deviation from linearity becomes evident, signifying plastic effects wherein cells undergo neighbor exchanges. However, these exchanges alone are insufficient to facilitate a viscous flow of cells into the micropipette. At higher pressures, the adhesive forces among cells fail to sustain aggregate cohesion, resulting in a visco-plastic flow of cells.

The delineation of these three distinct regimes, if validated in actual cellular contexts, holds promise for application in experiments aimed at detecting metastatic risks in tumors. In practical terms, considering a real sample of tumor cells in a micropipette aspiration experiment, a linear response to pressure akin to blood pressure suggests a relatively low risk of current metastasis through the bloodstream. Conversely, a nonlinear response may serve as an indicator of heightened risk, implying an increased likelihood of metastasis through the bloodstream.

A limitation of our cellular aggregate model is the computational burden imposed by the number of cells and simulation time. As these are extensive cells, a simple simulation with 500 cells, each composed of 50 particles, results in 25 000 particles. Due to the sensitivity of the potentials, a considerably small time step is required to prevent numerical divergences. This posed a significant challenge in conducting more in-depth analyses, such as investigating the relationship between micropipette size and cell size.

A suggestion for future analyses is to employ a model that omits consideration of cell shape, allowing for simulations with a significantly larger number of cells. By foregoing the inclusion of cell morphology, computational efficiency could be improved, enabling the exploration of a broader parameter space. This approach may facilitate a more comprehensive investigation into factors such as the influence of micropipette size and cell size on the system's behavior. Despite the simplification, such a model could still provide valuable insights into the fundamental dynamics of cellular aggregates in the context of micropipette aspiration.

Bibliography

Abbasi, M. et al. Erythrocyte-erythrocyte aggregation dynamics under shear flow. *Physical Review Fluids*, v. 6, n. 2, p. 023602, fev. 2021. Citado na página 54.

ÅSTRÖM, J. A.; KARTTUNEN, M. Cell aggregation: Packing soft grains. *Physical Review E - Statistical, Nonlinear, and Soft Matter Physics*, v. 73, n. 6, 2006. ISSN 15393755. Citado na página 19.

ÅSTRÖM, J. A.; LATVA-KOKKO, M.; TIMONEN, J. Dynamic rigidity transition. *Physical Review E - Statistical Physics, Plasmas, Fluids, and Related Interdisciplinary Topics*, v. 67, n. 1, p. 6, 2003. ISSN 1063651X. Citado na página 19.

BERG, H. C.; TURNER, L. *Movement of microorganisms in viscous environments [12].* 1979. 349–351 p. Citado na página 17.

BILLONI, O. V.; STARIOLO, D. A. Distributions of switching times of single-domain particles using a time quantified Monte Carlo method. *Journal of Magnetism and Magnetic Materials*, v. 316, n. 1, p. 49–53, 2007. ISSN 0304-8853. Disponível em: <https://www.sciencedirect.com/science/article/pii/S0304885307005628>. Citado na página 19.

BOEY, S. K.; BOAL, D. H.; DISCHER, D. E. Simulations of the erythrocyte cytoskeleton at large deformation. I. Microscopic models. *Biophysical Journal*, 1998. ISSN 00063495. Citado na página 20.

COUZIN, I. D. et al. Effective leadership and decision-making in animal groups on the move. *Nature*, v. 433, n. 7025, p. 513–516, 2005. ISSN 00280836. Citado na página 17.

DISCHER, D. E.; BOAL, D. H.; BOEY, S. K. Simulations of the erythrocyte cytoskeleton at large deformation. II. Micropipette aspiration. *Biophysical Journal*, 1998. ISSN 00063495. Citado na página 20.

EINSTEIN, A. Über die von der molekularkinetischen Theorie der Wärme geforderte Bewegung von in ruhenden Flüssigkeiten suspendierten Teilchen. *Annalen der Physik*, v. 322, n. 8, p. 549–560, 1905. ISSN 15213889. Citado na página 18.

ESTEBAN-MANZANARES, G. et al. Improved Measurement of Elastic Properties of Cells by Micropipette Aspiration and Its Application to Lymphocytes. *Annals of Biomedical Engineering*, 2017. ISSN 15739686. Citado na página 20.

EVANS, E. A. New Membrane Concept Applied to the Analysis of Fluid Shear- and Micropipette-Deformed Red Blood Cells. *Biophysical Journal*, 1973. ISSN 00063495. Citado na página 19.

FORTUNA, I. *Um Modelo Estocástico para a Migração de Células Individuais.* Tese (Doutorado) — Universidade Federal do Rio Grande do Sul, 2020. Citado na página 19.

GLAZIER, J. A.; GRANER, F. Simulation of the differential adhesion driven rearrangement of biological cells. *Physical Review E*, 1993. ISSN 1063651X. Citado na página 19.

GONZÁLEZ-BERMÚDEZ, B.; GUINEA, G. V.; PLAZA, G. R. Advances in Micropipette Aspiration: Applications in Cell Biomechanics, Models, and Extended Studies. *Biophysical Journal*, v. 116, n. 4, p. 587–594, 2019. ISSN 15420086. Citado na página 19.

GRANER, F.; GLAZIER, J. A. Simulation of biological cell sorting using a two-dimensional extended Potts model. *Physical Review Letters*, 1992. ISSN 00319007. Citado na página 19.

GUEVORKIAN, K. et al. Aspiration of biological viscoelastic drops. *Physical Review Letters*, mar 2010. ISSN 00319007. Disponível em: <http://arxiv.org/abs/1003.4372http://dx.doi.org/10.1103/PhysRevLett.104.218101>. Citado 2 vezes nas páginas 17 and 20.

GUEVORKIAN, K. et al. Mechanosensitive shivering of model tissues under controlled aspiration. *Proceedings of the National Academy of Sciences*, v. 108, n. 33, p. 13387–13392, aug 2011. ISSN 0027-8424. Disponível em: <http://www.pnas.org/cgi/doi/10.1073/pnas.1105741108>. Citado 3 vezes nas páginas 17, 19, and 20.

GUEVORKIAN, K.; MAÎTRE, J. L. Micropipette aspiration: A unique tool for exploring cell and tissue mechanics in vivo. *Methods in Cell Biology*, 2017. ISSN 0091679X. Citado 3 vezes nas páginas 17, 19, and 20.

GUILAK, F.; TEDROW, J. R.; BURGKART, R. Viscoelastic properties of the cell nucleus. *Biochemical and Biophysical Research Communications*, 2000. ISSN 0006291X. Citado na página 19.

GUTTAL, V.; COUZIN, I. D. Social interactions, information use, and the evolution of collective migration. Proceedings of the National Academy of Sciences. 107, 16172-16177. Guttal1 2010 Guttal1Supp 2010 Guttal1Appendix 2010. *Proceedings of the National Academy of Sciences*, v. 107, p. 16172–16177, 2010. Citado na página 17.

HAGA, H. et al. Collective movement of epithelial cells on a collagen gel substrate. *Biophysical Journal*, v. 88, n. 3, p. 2250–2256, 2005. ISSN 00063495. Citado na página 17.

HELBING, D.; MOLNÁR, P. Social force model for pedestrian dynamics. *Physical Review E*, 1995. ISSN 1063651X. Citado na página 17.

HOCHMUTH, R. M. Measuring the mechanical properties of individual human blood cells. *Journal of Biomechanical Engineering*, 1993. ISSN 15288951. Citado na página 17.

HOCHMUTH, R. M. *Micropipette aspiration of living cells*. 2000. Citado 2 vezes nas páginas 19 and 20.

J. Newman, T. Modeling Multicellular Systems Using Subcellular Elements. *Mathematical Biosciences and Engineering*, 2005. ISSN 1551-0018. Citado na página 19.

JONES, W. R. et al. Alterations in the young's modulus and volumetric properties of chondrocytes isolated from normal and osteoarthritic human cartilage. *Journal of Biomechanics*, 1999. ISSN 00219290. Citado na página 18.

LANDAU, L.; LIFCHTZ, E. *Theory de L'Élasticité*. Moscou: Editións MIR, 1967. Citado na página 24.

LYKOV, K. et al. Probing eukaryotic cell mechanics via mesoscopic simulations. *PLOS Computational Biology*, v. 13, n. 9, p. e1005726, sep 2017. ISSN 1553-7358. Disponível em: <https://dx.plos.org/10.1371/journal.pcbi.1005726>. Citado na página 20.

MAJKUT, S. et al. Heart-specific stiffening in early embryos parallels matrix and myosin expression to optimize beating. *Current Biology*, 2013. ISSN 09609822. Citado 2 vezes nas páginas 19 and 20.

MKRTCHYAN, A.; ÅSTRÖM, J.; KARTTUNEN, M. A new model for cell division and migration with spontaneous topology changes. *Soft Matter*, 2014. ISSN 17446848. Citado na página 19.

NAVA, A. et al. In vivo mechanical characterization of human liver. *Medical Image Analysis*, v. 12, n. 2, p. 203–216, 2008. ISSN 13618415. Citado 2 vezes nas páginas 19 and 20.

OBATA, T. et al. Fluctuations in human's walking. In: *AIP Conference Proceedings*. AIP, 2000. v. 519, p. 720–722. ISSN 0094243X. Disponível em: <http://aip.scitation.org/doi/abs/10.1063/1.1291648>. Citado na página 17.

OURIQUE, G.; TEIXEIRA, E.; BRUNNET, L. Modelling micropipette aspiration with active particles. *Physica A: Statistical Mechanics and its Applications*, v. 589, p. 126661, 2022. ISSN 0378-4371. Disponível em: <https://www.sciencedirect.com/science/article/pii/S0378437121008992>. Citado na página 20.

PLAZA, G. R. et al. Study of the influence of actin-binding proteins using linear analyses of cell deformability. *Soft Matter*, 2015. ISSN 17446848. Citado na página 20.

PORAZINSKI, S. et al. YAP is essential for tissue tension to ensure vertebrate 3D body shape. *Nature*, 2015. ISSN 14764687. Citado 2 vezes nas páginas 19 and 20.

RAMASWAMY, S. The Mechanics and Statistics of Active Matter. *Annual Review of Condensed Matter Physics*, 2010. ISSN 1947-5454. Citado na página 17.

REYNOLDS, C. W. FLOCKS, HERDS, AND SCHOOLS: A DISTRIBUTED BEHAVIORAL MODEL. *Computer Graphics (ACM)*, 1987. ISSN 00978930. Citado na página 17.

ROMANCZUK, P. et al. Active Brownian particles. *The European Physical Journal Special Topics*, 2012. ISSN 1951-6355. Citado na página 18.

SATO, M. et al. Application of the micropipette technique to the measurement of cultured porcine aortic endothelial cell viscoelastic properties. *Journal of Biomechanical Engineering*, v. 112, n. 3, p. 263–268, 1990. ISSN 15288951. Citado na página 19.

SULSKY, D.; CHILDRESS, S.; PERCUS, J. K. A model of cell sorting. *Journal of Theoretical Biology*, v. 106, n. 3, p. 275–301, 1984. ISSN 10958541. Citado na página 18.

SUMPTER, D. et al. Information transfer in moving animal groups. In: *Theory in Biosciences*. [S.l.: s.n.], 2008. v. 127, n. 2, p. 177–186. ISSN 14317613. Citado na página 17.

SWAT, M. H. et al. Multi-Scale Modeling of Tissues Using CompuCell3D. In: *Methods in Cell Biology*. [S.l.: s.n.], 2012. v. 110, p. 325–366. Citado na página 19.

SZABÓ, B. et al. Phase transition in the collective migration of tissue cells: Experiment and model. *Physical Review E - Statistical, Nonlinear, and Soft Matter Physics*, v. 74, n. 6, p. 1–6, 2006. ISSN 15393755. Citado 3 vezes nas páginas 18, 31, and 33.

TEIXEIRA, E. F.; FERNANDES, H. C. M.; BRUNNET, L. G. Extended Cell Model for Active Matter: Single Cell Phase diagram. *Manuscript in preparation*, 2020. Citado na página 54.

TEIXEIRA, E. F.; FERNANDES, H. C. M.; BRUNNET, L. G. Single Active Ring Model. *arXiv*, feb 2021. Disponível em: <http://arxiv.org/abs/2102.03439>. Citado 8 vezes nas páginas 19, 20, 29, 30, 31, 35, 41, and 43.

THERET, D. P. et al. The application of a homogeneous half-space model in the analysis of endothelial cell micropipette measurements. *Journal of Biomechanical Engineering*, v. 110, n. 3, p. 190–199, 1988. ISSN 15288951. Citado 5 vezes nas páginas 20, 23, 24, 25, and 44.

TLILI, S. et al. Colloquium: Mechanical formalisms for tissue dynamics. *The European Physical Journal E*, Springer Science and Business Media LLC, v. 38, n. 5, maio 2015. Disponível em: <https://doi.org/10.1140/epje/i2015-15033-4>. Citado na página 25.

TLILI, S. L.; GRANER, F.; DELANOE-AYARI, H. A microfluidic platform to investigate the role of mechanical constraints on tissue reorganization. *Development*, v. 149, n. 20, p. dev200774, 11 2022. ISSN 0950-1991. Disponível em: <https://doi.org/10.1242/dev.200774>. Citado na página 9.

WELIKY, M.; OSTER, G. The mechanical basis of cell rearrangement. I. Epithelial morphogenesis during Fundulus epiboly. *Development*, v. 109, n. 2, p. 373–386, 1990. ISSN 09501991. Citado na página 18.

WU, J. Z.; HERZOG, W.; EPSTEIN, M. Modelling of location- and time-dependent deformation of chondrocytes during cartilage loading. *Journal of Biomechanics*, 1999. ISSN 00219290. Citado na página 20.

ZHOU, E. H.; LIM, C. T.; QUEK, S. T. Finite element simulation of the micropipette aspiration of a living cell undergoing large viscoelastic deformation. *Mechanics of Advanced Materials and Structures*, 2005. ISSN 15376494. Citado na página 20.